



**Neutral iridium(III) complexes bearing  
 BODIPY–substituted N–heterocyclic carbene (NHC) ligands:  
 synthesis, photophysics, in vitro theranostic photodynamic  
 therapy, and antimicrobial activity**

Journal:	<i>Photochemical &amp; Photobiological Sciences</i>
Manuscript ID	PP-ART-03-2019-000142.R2
Article Type:	Paper
Date Submitted by the Author:	05-Aug-2019
Complete List of Authors:	Liu, Bingqing; North Dakota State University, Monro, Susan; Acadia University Javed, Mohammed; North Dakota State University Cameron, Collin; University of North Carolina at Greensboro Colon, Katsuya; University of North Carolina at Greensboro Xu, Wan; North Dakota State University, Chemistry and Biochemistry Kilina, Svetlana; North Dakota State University, Chemistry and Biochemistry McFarland, Sherri; University of North Carolina at Greensboro, Sun, Wenfang; North Dakota State University, Chemistry and Biochemistry

## ARTICLE

# Neutral iridium(III) complexes bearing BODIPY-substituted *N*-heterocyclic carbene (NHC) ligands: synthesis, photophysics, *in vitro* theranostic photodynamic therapy, and antimicrobial activity

Received 00th January 20xx,  
Accepted 00th January 20xx

DOI: 10.1039/x0xx00000x

Bingqing Liu,<sup>a</sup> Susan Monro,<sup>b</sup> Mohammed A. Javed,<sup>a</sup> Colin G. Cameron,<sup>c</sup> Katsuya L. Colón,<sup>c</sup> Wan Xu,<sup>a</sup> Svetlana Kilina,<sup>a</sup> Sherri A. McFarland,<sup>\*bc</sup> and Wenfang Sun<sup>\*a</sup>

The synthesis, photophysics, and photobiological activities of a series of novel neutral heteroleptic cyclometalated iridium(III) complexes incorporating boron dipyrromethene (BODIPY) substituted *N*-heterocyclic carbene (NHC) ligands (**Ir1** – **Ir5**) are reported. The effect of the substitution position of BODIPY on the NHC ligands, either on C4 of the phenyl ring (**Ir1** – **Ir3**) or C5 of the benzimidazole unit (**Ir4** and **Ir5**), and its linker type (single or triple bond) on the photophysical properties was studied. **Ir1** – **Ir5** exhibited BODIPY-localized intense <sup>1</sup>L (intraligand transition) / <sup>1</sup>MLCT (metal-to-ligand charge transfer) absorption at 530–543 nm and <sup>1</sup>L/<sup>3</sup>CT (charge transfer) emission at 582–610 nm. The nanosecond transient absorption results revealed that the lowest triplet excited states of these complexes were the BODIPY-localized <sup>3</sup>π,π\* states. Complexes **Ir4** and **Ir5** exhibited blue-shifted <sup>1</sup>L absorption and <sup>1</sup>L/<sup>3</sup>CT emission bands compared to the corresponding absorption and emission bands in complexes **Ir1** and **Ir3**. However, replacing the methyl substituents on N3 of benzimidazole in complexes **Ir1** and **Ir4** with oligoether substituents in **Ir3** and **Ir5**, respectively, did not impact the energies of the low-energy absorption and emission bands in the corresponding complexes. Water-soluble complexes **Ir3** and **Ir5** have been explored as photosensitizers for *in vitro* photodynamic therapy (PDT) effects toward human SKMEL28 melanoma cells. **Ir3** showed no dark cytotoxicity (EC<sub>50</sub> >300 μM) but good photocytotoxic activity (9.66 ± 0.28 μM), whereas **Ir5** exhibited a higher dark cytotoxicity (20.2 ± 1.26 μM) and excellent photocytotoxicity (0.15 ± 0.01 μM). The phototherapeutic indices with visible light (400–700 nm) activation were >31 for **Ir3** and 135 for **Ir5**. **Ir3** and **Ir5** displayed <sup>1</sup>O<sub>2</sub> quantum yields of 38% and 22% in CH<sub>3</sub>CN, respectively, upon 450 nm excitation. **Ir5** was more effective at generating reactive oxygen species (ROS) *in vitro*. **Ir5** was also active against *Staphylococcus aureus* upon visible light activation, with a phototherapeutic index of >15 and EC<sub>50</sub> value of 6.67 μM. These photobiological activities demonstrated that these neutral Ir(III) complexes are promising *in vitro* PDT reagents, and substitution at C5 on the benzimidazole group of the NHC ligand was superior to C4 substitution on the phenyl ring.

## 1. Introduction

Photodynamic therapy (PDT) is an emerging cancer treatment modality that combines a photosensitizer (PS), oxygen, and light to destroy tumors and tumor vasculature and induce an immune response.<sup>1–5</sup> PDT is inherently selective because toxicity is confined to regions where the PS, oxygen, and light overlap

spatiotemporally.<sup>3,6,7</sup> During PDT, reactive oxygen species (ROS) are formed through energy (type II) or electron transfer (type I) reactions that take place between ground state molecular oxygen and the excited triplet state of the PS. The most important mediator of the PDT effect is thought to be singlet oxygen (<sup>1</sup>O<sub>2</sub>) produced through the type II PDT mechanism, but superoxide (O<sub>2</sub><sup>•-</sup>) or hydroxyl radical (<sup>•</sup>OH), generated by the type I PDT mechanism may also play a role.

Certain transition metal complexes are among the numerous PSs that have been explored due to their (1) interesting photophysical properties, (2) reduced photobleaching, and (3) improved kinetic stabilities (compared to organic PSs).<sup>8</sup> Among the metal complexes, Ru(II) systems are probably the most widely studied for PDT.<sup>9,10</sup> Our Ru(II) complex TLD1433,<sup>10,11</sup> which incorporates a π-expansive ligand derived from imidazo[4,5-*f*][1,10]phenanthroline appended to an α-terthienyl unit, just successfully completed a Phase 1b

<sup>a</sup> Department of Chemistry and Biochemistry, North Dakota State University, Fargo, ND 58108–6050, USA. E-mail: Wenfang.Sun@ndsu.edu

<sup>b</sup> Department of Chemistry, Acadia University, 6 University Avenue, Wolfville, NS B4P 2R6, Canada.

<sup>c</sup> Department of Chemistry and Biochemistry, University of North Carolina at Greensboro, Greensboro, NC 27402–6170, USA. E-mail: samcfarl@uncg.edu

† Electronic Supplementary Information (ESI) available: Details for the photobiological activity studies; natural transition orbitals (NTOs) representing transitions contributing to the absorption bands of **Ir1**–**Ir5** in toluene; solvent-dependent UV-vis absorption and emission spectra at r.t. for **Ir1**–**Ir5**; emission characteristics in different solvents at r.t. for **Ir1**–**Ir5**; comparison of the emission spectra in air-saturated and deaerated (degassed with N<sub>2</sub> for 40 min) toluene solution of **Ir2**–**Ir5**; and time-resolved nanosecond transient absorption spectra of **Ir1**–**Ir5** in toluene. See DOI: 10.1039/x0xx00000x

clinical trial for treating bladder cancer with PDT (ClinicalTrials.gov Identifier: NCT03053635). This example demonstrates the utility of lowest-energy  $\pi, \pi^*$  triplet states, in this case centered on the oligothieryl unit, with extremely long lifetimes for highly efficient photosensitization.

Some transition-metal complexes possess the distinct advantage of having singlet and triplet excited states that can be tuned independently for optimization of their respective characteristics when appropriate  $\pi$ -conjugated ligands are chosen. We have reported that it is possible to shift the singlet charge-transfer absorption to longer wavelengths (for activation by red wavelengths of light) by extending the  $\pi$ -conjugation of the organic ligands, while allowing the lowest triplet excited state ( $T_1$ ) to be localized on the  $\pi$ -expansive organic ligands.<sup>12</sup> The  $\pi, \pi^*$  nature of the lowest triplet excited state results in very long triplet excited state lifetimes, which have the potential to facilitate ROS production even at low oxygen tension. Unlike organic PSs, metal complexes possess high quantum yields for triplet state formation due to the heavy atom effect (metal-induced rapid ISC), and their triplet excited states are typically long-lived. All of these properties are desirable features for next-generation PSs.

Ir(III) complexes are also of interest because some have exhibited high efficiency for ROS production *via* electron or energy transfer.<sup>14</sup> Many Ir(III) complexes possess high quantum yields for triplet excited state formation and long-lived triplet excited states for efficient ROS generation even under hypoxia.<sup>13</sup> It has been reported that cationic Ir(III) complexes can target mitochondria,<sup>14-18</sup> lysosomes,<sup>19,20</sup> the endoplasmic reticulum,<sup>21,22</sup> or nuclei<sup>23,24</sup> in a variety of cancer cell lines. A mitochondria-targeted Ir(III) complex PS was reported to show improved PDT effects under hypoxia.<sup>14</sup> These complexes can also display bright intracellular luminescence, imparting theranostic capacity.<sup>13-20,23-25</sup> Therefore, Ir(III) complexes have emerged as a new platform for theranostic PDT applications. However, most of the currently studied Ir(III) complexes absorb light maximally in the UV to blue spectral regions, wavelengths of lesser interest for PDT because of their shallow tissue penetration due to tissue scattering and absorption.<sup>26</sup>

Although it is possible to red-shift the charge transfer ground-state absorption bands of the cyclometalating monocationic Ir(III) complexes  $[\text{Ir}(\text{C}^{\wedge}\text{N})_2(\text{N}^{\wedge}\text{N})]^+$  (where  $\text{N}^{\wedge}\text{N}$  refers to the diimine ligand and  $\text{C}^{\wedge}\text{N}$  refers to the cyclometalating ligand) to longer wavelength by introducing electron-withdrawing substituents on the diimine ligands<sup>27</sup> or through benzannulation at the diimine ligands, the molar extinction coefficients of the charge transfer absorption bands are quite low and the lowest triplet excited state ( $T_1$ ) lifetimes become much shorter (tens of ns).<sup>28-32</sup> In contrast, it has been shown that bichromophoric transition-metal complexes with  $\pi$ -conjugated organic chromophores result in long-lived  $^3\pi, \pi^*$   $T_1$  states localized at the organic chromophore with simultaneous red-shifting of the ground-state absorption to the longer wavelengths. Metal coordination improves  $\pi$ -conjugation across the organic ligands through planarization, facilitating the interactions between ligands. It also increases the quantum yield of triplet excited-state formation *via* heavy atom induced

ISC. Such a strategy has been applied in TLD1433<sup>10</sup> and other Ru(II) complexes for PDT applications,<sup>11,33-39</sup> but is relatively rare for Ir(III) systems.<sup>40-44</sup>

Borondipyrromethene (BODIPY) and its derivatives, a class of strong light-harvesting fluorophores with facile wavelength tunability, have been extensively explored as potential PSs for PDT applications in recent years.<sup>45-48</sup> For example, Dong and co-workers have demonstrated that nanoparticles encapsulating BODIPY or aza-BODIPY derivatives bearing diethylaminophenyl or dimethylaminophenyl substituents exhibited very strong pH-triggered photodynamic and photothermal therapy for HeLa cells and HeLa tumor bearing nude mice.<sup>47,48</sup> Moreover, BODIPY appears as a promising moiety to be attached to a monodentate or polydentate ligand to tune the absorption wavelength of the transition-metal PSs to the desired spectral region.<sup>39-41,49</sup> However, BODIPY-Ir(III) dyads for PDT applications are not well-studied.<sup>40,41,49</sup> One of the few examples used BODIPY tethered cationic cyclometalated Ir(III) dyads as PSs for PDT and bioimaging applications, and their *in vitro* PDT effects were marginal due to high dark toxicity ( $\text{IC}_{50} = 8.16 - 16.70 \mu\text{M}$  toward 1121 or LLC cell lines). Phototherapeutic index (PI) values (1.3-3.8) were very small.<sup>40,41</sup>

Recently, *N*-heterocyclic carbene (NHC) based iridium(III) complexes have attracted great interest.<sup>50-54</sup> Unlike the numerous well-studied monocationic cyclometalated Ir(III) complexes  $[\text{Ir}(\text{C}^{\wedge}\text{N})_2(\text{N}^{\wedge}\text{N})]^+$  (where  $\text{N}^{\wedge}\text{N}$  refers to the diimine ligand and  $\text{C}^{\wedge}\text{N}$  refers to the cyclometalating ligand), monoanionic NHC ligands, such as 1-phenyl-3-alkylbenzimidazole, as the  $\text{N}^{\wedge}\text{N}$  ligand gives rise to neutral complexes.<sup>54,55</sup> To date, NHC-Ir(III) complexes have largely been studied for their catalytic<sup>50</sup> and optoelectronic applications.<sup>51-54</sup> Biological activities were only reported on monocationic Ir(III) complexes with bis(alkylated-NHC) ligands,<sup>15,50</sup> which possessed high dark toxicity and could only be activated by UV light (365 nm). To date, the biological activities of the neutral  $\text{Ir}(\text{C}^{\wedge}\text{N})_2(\text{NHC})$  complexes remain unexplored.

Herein, a series of neutral iridium(III) complexes bearing BODIPY-NHC ligands (Chart 1) were designed and synthesized to explore their photophysical properties and *in vitro* PDT effects. These complexes all contain benzo[*h*]quinoline (*bhq*) as the cyclometalating ligands, but the NHC ligand varies from 1-(4-BODIPY-ethynylphenyl)-3-methyl-1*H*-benzo[*d*]imidazole-3-iumiodide (**L1**), 1-(4-BODIPY-phenyl)-3-methyl-1*H*-benzo[*d*]imidazole-3-iumiodide (**L2**), 1-(4-BODIPY-ethynylphenyl)-3-(2-(2-(2-methoxyethoxy)ethoxy)ethyl)-1*H*-benzo[*d*]imidazole-3-iumiodide (**L3**), 5-(4-BODIPY-ethynylphenyl)-3-methyl-1*H*-benzo[*d*]imidazole-3-iumiodide (**L4**), to 5-(4-BODIPY-ethynylphenyl)-3-(2-(2-(2-methoxyethoxy)ethoxy)ethyl)-1*H*-benzo[*d*]imidazole-3-iumiodide (**L5**). BODIPY was incorporated into the NHC ligand scaffold at different sites through a single bond (**Ir2**) or a triple bond (**Ir1** and **Ir3-Ir5**) in order to red-shift the absorption of the complexes to longer wavelengths. An oligoether chain, 2-(2-(2-methoxyethoxy)ethoxy)ethyl, was appended to **Ir3**

and **Ir5** to increase the hydrophilicity of the neutral complexes. The photophysical properties of these five complexes were systematically investigated by various spectroscopic methods and simulated by density functional theory (DFT) calculations. The *in vitro* theranostic PDT effects of the two water-soluble complexes **Ir3** and **Ir5** were investigated. The impact of the BODIPY attachment site on the photophysics and PDT effects of these dyads was explored.

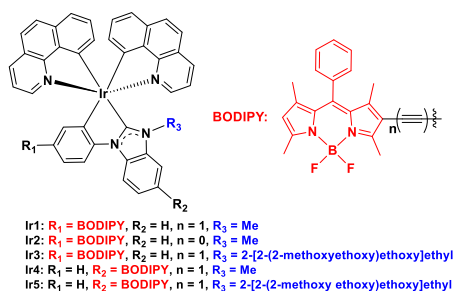
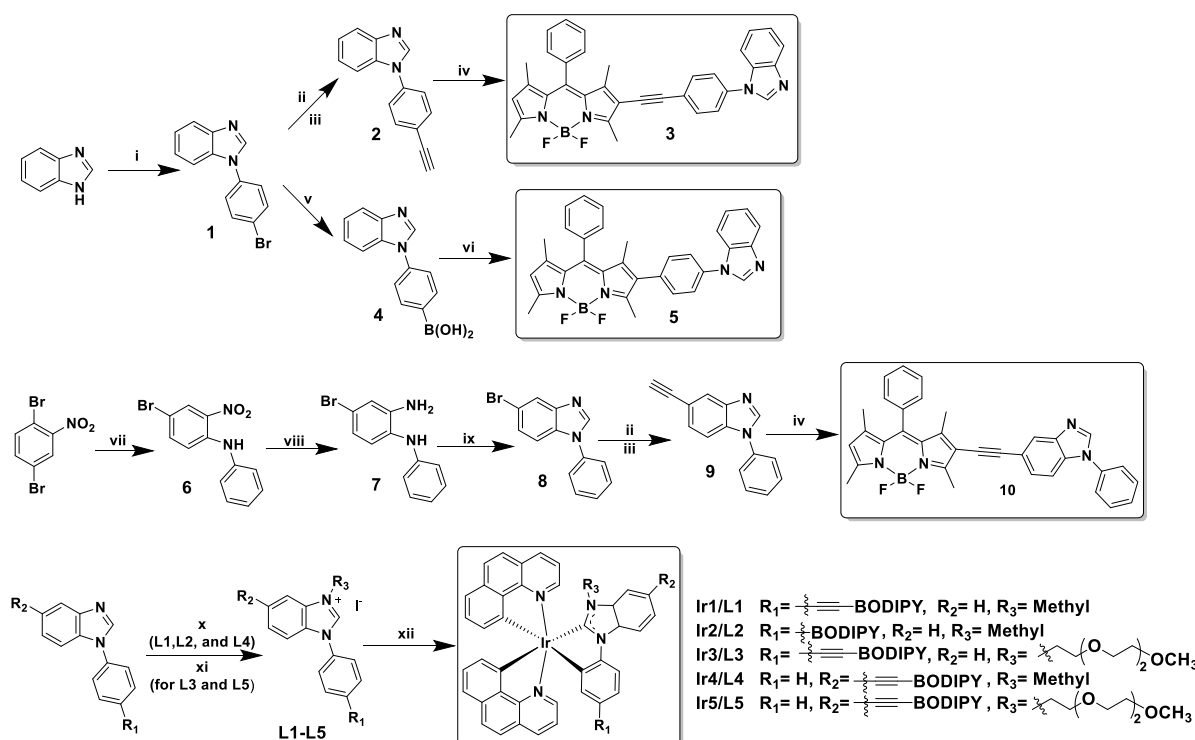


**Chart 1.** Structures of BODIPY-NHC-Ir(III) Complexes **Ir1–Ir5**.

## 2. Experiments section

### 2.1. Materials and synthesis

All reagents and solvents were purchased from Alfa Aesar and VWR International and used as received.  $\text{Al}_2\text{O}_3$  gels (activated, neutral) and silica gels (230–400 mesh) for column chromatography were purchased from Sorbent Technology. Benzo[*h*]quinoline (C<sup>N</sup> ligand) was obtained from Alfa–Aesar and its Ir(III)  $\mu$ -chloro-bridged dimers  $[\text{Ir}(\text{C}^{\text{N}})_2\text{Cl}]_2$  was synthesized according to the literature procedure.<sup>56</sup> Compounds 1-(4-bromophenyl)-1*H*-benzimidazole (compound **1** in Scheme 1),<sup>57</sup> 4-bromo-2-nitro-*N*-phenylaminobenzene (compound **6** in Scheme 1),<sup>58</sup> 4-bromo-*N*<sup>1</sup>-phenyl-1,2-benzenediamine (compound **7** in Scheme 1),<sup>59</sup> and 2-iodo-BODIPY<sup>60</sup> were synthesized following the reported procedures. The synthetic route for the synthesis of ligands **L1–L5** and complexes **Ir1–Ir5** are provided in Scheme 1. <sup>1</sup>H NMR, high-resolution mass spectrometry (HRMS), and elemental analyses were used to characterize these complexes. <sup>1</sup>H NMR spectra were obtained on a Varian Oxford-400 or Bruker-400 spectrometer in  $\text{CDCl}_3$  using tetramethylsilane (TMS) as the internal standard. Bruker BioTOF III mass spectrometer was used for ESI–HRMS analyses. NuMega Resonance Laboratories, Inc. in San Diego, California conducted elemental analyses.



**Scheme 1.** Synthetic Route for Ligands **L1–L5** and Complexes **Ir1–Ir5**. Reagents and conditions: (i) 1-bromo-4-iodobenzene, CuI,  $\text{Cs}_2\text{CO}_3$ , 1,10-phenanthroline, DMF, 110 °C, 40 hrs.; (ii) CuI,  $\text{PdCl}_2(\text{PPh}_3)_2$ , ethynyltrimethylsilane, TEA/dioxane, 100 °C, 1 hr.; (iii) TBAF, THF, 0 °C, 1 hr.; (iv) 2-Iodo-BODIPY, CuI,  $\text{Pd}(\text{PPh}_3)_4$ , TEA, THF, 50 °C, 16 hrs.; (v) triisopropyl borate, <sup>n</sup>BuLi, anhydrous THF, –78 °C, 1 hr., then r.t. overnight, followed by HCl, 100 °C, 1 hr.; (vi) 2-iodo-BODIPY,  $\text{K}_2\text{CO}_3$ ,  $\text{Pd}(\text{PPh}_3)_4$ , toluene, THF, water, 70 °C, overnight; (vii) NaOAc, aniline, 160 °C, 7 hrs.; (viii)  $\text{Na}_2\text{S}$ , S, water, reflux, 6 hrs.; (ix) formic acid, 100 °C, overnight; (x) MeI, THF, 100 °C, 24 hrs.; (xi) 1-iodo-3,6,9-trioxadecane, toluene, 100 °C, 96 hrs.; (xii)  $[\text{Ir}(\text{benzo}[h]\text{quinoline})_2(\mu\text{-Cl})_2]$ ,  $\text{Ag}_2\text{O}$ , 1,2-dichloroethane, reflux, 24 hrs.

### 2.2. Synthesis of precursor compounds 2–5 and 8–10

**Compound 2.** A solution of **1** (544 mg, 2 mmol), CuI (19 mg, 0.1 mmol),  $\text{PdCl}_2(\text{PPh}_3)_2$  (70 mg, 0.1 mmol) in trimethylamine

(TEA)/dioxane (2:1, v/v) was degassed with N<sub>2</sub> at room temperature for 20 minutes. Then, ethynyltrimethylsilane (0.86 mL, 6 mmol) was added and the resulting reaction mixture was heated at 100 °C for 1 hour under N<sub>2</sub>. After cooling to room temperature, the mixture was concentrated and purified by column chromatography over silica gel using hexane:ethyl acetate = 1:2 (v/v) as the eluent to give product as pale yellow solid. This pale yellow solid (500 mg, 1.8 mmol) was dissolved in THF (10 mL), and THF solution of tetrabutylammonium fluoride (TBAF) (10 mL, 1 M in THF) was added at 0 °C. The reaction mixture was stirred at room temperature for 1 hour. Then the solution was diluted with ethyl acetate (EA) and washed with water and brine consequently. The organic layer was dried over Na<sub>2</sub>SO<sub>4</sub> and concentrated. The residue was purified by column chromatography over silica gel using hexane:ethyl acetate=1:2 (v/v) as the eluent to give compound **2** as pale yellow solid (360 mg, 81%). <sup>1</sup>H NMR (400 MHz, CDCl<sub>3</sub>) δ 8.14 (s, 1H), 7.91 (dd, *J* = 6.4, 2.7 Hz, 1H), 7.73 (d, *J* = 8.4 Hz, 2H), 7.57 (dd, *J* = 6.6, 2.7 Hz, 1H), 7.53 (d, *J* = 8.4 Hz, 2H), 7.43–7.34 (m, 2H), 3.22 (s, 1H).

**Compound 3.** The solution of 2-iodo-BODIPY (200 mg, 0.44 mmol), compound **2** (97 mg, 0.44 mmol), CuI (17 mg, 0.09 mmol), and Pd(PPh<sub>3</sub>)<sub>4</sub> (57 mg, 0.049 mmol) in 10 mL degassed mixed solvent (THF/TEA = 4/1) was heated to 50 °C and stirred for 16 hours in dark. After cooling to room temperature, the solvent was removed under reduced pressure and the residue was extracted with CH<sub>2</sub>Cl<sub>2</sub> and washed with brine. After removal of the solvent from the organic layer, the crude product was purified by flash column chromatography with CH<sub>2</sub>Cl<sub>2</sub>/acetone (v/v = 50/1) being used as the eluent to obtain a dark red solid (200 mg, 83%). <sup>1</sup>H NMR (400 MHz, with CDCl<sub>3</sub>) δ 8.14 (s, 1H), 7.94–7.86 (m, 1H), 7.67 (d, *J* = 8.4 Hz, 2H), 7.62–7.44 (m, 6H), 7.43–7.30 (m, 4H), 6.08 (s, 1H), 2.75 (s, 3H), 2.62 (s, 3H), 1.55 (s, 3H), 1.44 (s, 3H).

**Compound 4.** Under -78 °C, <sup>n</sup>BuLi (0.5 mL, 2.5 M in hexane) was added dropwise to the solution of compound **1** (151 mg, 0.56 mmol) and B(O<sup>i</sup>Pr)<sub>3</sub> (157 mg, 0.83 mmol) in THF (10 mL). The mixture was stirred at -78°C for 1 h, and then allowed to warm up to room temperature, and continued stirring for overnight. The reaction was quenched by addition of concentrated aqueous NH<sub>4</sub>Cl (10 mL), and the volatiles were evaporated in vacuum. Then, HCl (10 mL, 37% aq.) was added to the solution and the resultant mixture was heated to reflux for 1 h. After cooling to room temperature, the mixture was carefully adjusted to pH=7 with NaOH. The white suspension was extracted with CH<sub>2</sub>Cl<sub>2</sub>. After removal of the solvent, the residue was dried under vacuum. The crude product was purified by column chromatography on silica gel and eluted with acetone to obtain white solid as the product (47 mg, 36%). <sup>1</sup>H NMR (400 MHz, DMSO) δ 8.60 (s, 1H), 8.24 (s, 1H), 8.04 (d, *J* = 8.0 Hz, 2H), 7.79 (d, *J* = 7.4 Hz, 1H), 7.67 (d, *J* = 7.9 Hz, 2H), 7.34 (dt, *J* = 13.6, 6.8 Hz, 2H).

**Compound 5.** A solution of compound **4** (44 mg, 0.18 mmol), 2-iodo-BODIPY (56 mg, 0.12 mmol), and K<sub>2</sub>CO<sub>3</sub> (166 mg, 1.2 mmol) in toluene (8 mL), THF (8 mL), and water (2 mL) was degassed with N<sub>2</sub> at room temperature for 20 minutes. After that, Pd(PPh<sub>3</sub>)<sub>4</sub> (3 mg, 0.0025 mmol) was added, and the

mixture was heated to 70 °C for overnight. After evaporation of the volatiles under reduced pressure, water (10 mL) was added, and the mixture was extracted with CH<sub>2</sub>Cl<sub>2</sub> (3×10 mL). The combined organic layers were washed with brine (100 mL), and dried over anhydrous MgSO<sub>4</sub>. The solvent was then removed, and the crude product was purified by column chromatography on silica gel using hexane/ethyl acetate (v/v = 1:1) as the eluent to obtain orange solid as the target compound (79 mg, 78%). <sup>1</sup>H NMR (400 MHz, CDCl<sub>3</sub>) δ 8.13 (d, *J* = 7.5 Hz, 1H), 7.92–7.84 (m, 1H), 7.62–7.45 (m, 7H), 7.40–7.29 (m, 5H), 6.04 (s, 1H), 2.61 (s, 3H), 2.59 (s, 3H), 1.41 (s, 3H), 1.36 (s, 3H).

**Compound 8.** The mixture of compound **7** (880 mg, 3.36 mmol) and formic acid (20 mL) was stirred at 100 °C for overnight. The reaction mixture was cooled to room temperature and concentrated under reduced pressure to afford a crude solid. The crude solid was partitioned between ethyl acetate (250 mL) and NH<sub>3</sub>/H<sub>2</sub>O (25 mL). The ethyl acetate layer was combined, dried with Na<sub>2</sub>SO<sub>4</sub>, and then concentrated under reduced pressure. The residue was purified by column chromatography (silica gel, eluted with CH<sub>2</sub>Cl<sub>2</sub>) to get the target compound as off-white solid (860 mg, 98%). <sup>1</sup>H NMR (400 MHz, CDCl<sub>3</sub>) δ 8.10 (s, 1H), 8.02 (d, *J* = 1.5 Hz, 1H), 7.59 (dd, *J* = 8.2, 7.4 Hz, 2H), 7.52–7.47 (m, 3H), 7.46–7.36 (m, 2H).

**Compound 9.** Following the similar synthetic procedure for compound **2**, compound **9** was obtained with 87% yield using compound **8** as the starting material. <sup>1</sup>H NMR (400 MHz, CDCl<sub>3</sub>) δ 8.13 (s, 1H), 8.06–7.96 (m, 1H), 7.59 (dd, *J* = 10.0, 5.5 Hz, 2H), 7.49 (dd, *J* = 11.7, 5.7 Hz, 4H), 7.42 (dt, *J* = 13.5, 5.1 Hz, 1H), 3.07 (s, 1H).

**Compound 10.** Following the similar synthetic procedure for compound **3**, compound **10** was obtained with 41% yield using compound **9** as the starting material. <sup>1</sup>H NMR (500 MHz, CDCl<sub>3</sub>) δ 8.14 (s, 1H), 7.97 (s, 1H), 7.59 (t, *J* = 7.7 Hz, 2H), 7.54–7.45 (m, 7H), 7.42 (d, *J* = 8.4 Hz, 1H), 7.33–7.28 (m, 2H), 6.03 (s, 1H), 2.74 (s, 3H), 2.59 (s, 3H), 1.54 (s, 3H), 1.41 (s, 3H).

### 2.3. General synthetic procedure for ligands L1–L5.

In a round-bottom flask equipped with a gastight Teflon cap, the precursor NHCs compound **3**, **5**, or **10** (1 mmol) was dissolved in 10 mL of THF (for synthesizing **L1**, **L2**, or **L4**) or in 1 mL of toluene (for synthesizing **L3** and **L5**). Then 1.5 mmol CH<sub>3</sub>I (for synthesizing **L1**, **L2**, or **L4**) or 1-iodo-3,6,9-trioxadecane (for synthesizing **L3** and **L5**) was added. The mixture was heated to 100 °C for 24 h. After the reaction, the solution was allowed to cool to room temperature. The formed precipitate was collected by filtration and washed with THF, dichloroethane, and Et<sub>2</sub>O (10 mL × 2) to obtain the corresponding target compound.

**L1.** A dark red powder was obtained as the product (yield: 73%). <sup>1</sup>H NMR (400 MHz, DMSO) δ 10.16 (s, 1H), 8.18 (d, *J* = 8.4 Hz, 1H), 8.05–7.71 (m, 8H), 7.65 (d, *J* = 3.7 Hz, 2H), 7.46–7.40 (m, 2H), 6.39 (s, 1H), 4.20 (s, 3H), 2.66 (s, 3H), 2.56 (s, 3H), 1.53 (s, 3H), 1.43 (s, 3H).

**L2.** A red powder was obtained as the product (yield: 67%). <sup>1</sup>H NMR (400 MHz, DMSO) δ 10.15 (s, 1H), 8.16 (d, *J* = 8.2 Hz, 1H), 7.94–7.69 (m, 6H), 7.63 (dd, *J* = 12.4, 7.5 Hz, 4H), 7.46 (d, *J*

= 7.6 Hz, 2H), 6.29 (s, 1H), 4.17 (s, 3H), 2.52 (s, 3H), 2.50 (s, 3H), 1.38 (s, 3H), 1.36 (s, 3H).

**L3.** A dark red powder was obtained as the product (yield: 53%). <sup>1</sup>H NMR (500 MHz, CDCl<sub>3</sub>) δ 10.72 (s, 1H), 7.97 (d, *J* = 7.6 Hz, 1H), 7.88 (d, *J* = 8.7 Hz, 2H), 7.74–7.66 (m, 4H), 7.53 (dd, *J* = 5.0, 1.9 Hz, 2H), 7.33–7.27 (m, 4H), 6.07 (s, 1H), 5.09–5.03 (m, 2H), 4.22–4.14 (m, 2H), 3.74 (dd, *J* = 5.5, 3.4 Hz, 2H), 3.60 (dd, *J* = 5.4, 3.5 Hz, 2H), 3.54 (dd, *J* = 5.6, 3.7 Hz, 2H), 3.41 (dd, *J* = 5.6, 3.7 Hz, 2H), 3.28 (s, 3H), 2.73 (s, 3H), 2.60 (s, 3H), 1.53 (s, 3H), 1.42 (s, 3H).

**L4.** A dark red powder was obtained as the product (yield: 58%). <sup>1</sup>H NMR (400 MHz, DMSO) δ 10.17 (s, 1H), 8.36 (s, 1H), 7.82–7.73 (m, 7H), 7.62 (d, *J* = 3.6 Hz, 3H), 7.53–7.34 (m, 2H), 6.37 (s, 1H), 4.17 (s, 3H), 2.66 (s, 3H), 2.54 (s, 3H), 1.52 (s, 3H), 1.41 (s, 3H).

**L5.** A dark red powder was obtained as the product (yield: 65%). <sup>1</sup>H NMR (400 MHz, CDCl<sub>3</sub>) δ 10.61 (s, 1H), 8.19 (s, 1H), 7.97–7.88 (m, 3H), 7.79–7.68 (m, 4H), 7.64–7.54 (m, 4H), 7.35–7.30 (m, 1H), 6.10 (s, 1H), 5.08–4.98 (m, 2H), 4.24–4.14 (m, 2H), 3.81–3.72 (m, 2H), 3.67–3.61 (m, 2H), 3.54 (dd, *J* = 5.4, 3.6 Hz, 2H), 3.45 (dd, *J* = 5.7, 3.7 Hz, 2H), 3.30 (s, 3H), 2.75 (s, 3H), 2.63 (s, 3H), 1.56 (s, 3H), 1.45 (s, 3H).

#### 2.4. General synthetic procedure for iridium complexes Ir1–Ir5.

The mixture of the NHC ligand (**L1–L5**, 0.12 mmol), [Ir(benzo[*h*]quinoline)<sub>2</sub>(μ-Cl)]<sub>2</sub> (76 mg, 0.06 mmol), Ag<sub>2</sub>O (56 mg, 0.24 mmol), and 1,2-dichloroethane (15 mL) was heated to reflux in the dark for 24 h. After the mixture was cooled to room temperature, the solvent was removed under reduced pressure to afford the crude product. Purification of the crude product was carried out on silica gel column chromatography eluted with CH<sub>2</sub>Cl<sub>2</sub>. The obtained product was further recrystallized in CH<sub>2</sub>Cl<sub>2</sub> / hexane to give the desired pure complex.

**Ir1.** A dark purple powder was obtained as the product (yield: 32%). <sup>1</sup>H NMR (400 MHz, CDCl<sub>3</sub>) δ 8.39 (d, *J* = 5.2 Hz, 1H), 8.27 (d, *J* = 5.2 Hz, 1H), 8.17 (d, *J* = 8.2 Hz, 1H), 8.03 (dd, *J* = 12.1, 7.6 Hz, 2H), 7.85–7.66 (m, 3H), 7.57–7.46 (m, 4H), 7.39–7.21 (m, 9H), 7.18–6.99 (m, 4H), 6.87 (s, 1H), 6.74 (d, *J* = 6.9 Hz, 1H), 6.33 (d, *J* = 7.0 Hz, 1H), 5.98 (s, 1H), 3.26 (s, 3H), 2.55 (s, 3H), 2.53 (s, 3H), 1.36 (s, 3H), 1.33 (s, 3H). ESI-HRMS (*m/z*): calcd. for [C<sub>61</sub>H<sub>44</sub>BF<sub>2</sub>IrN<sub>6</sub>+H]<sup>+</sup>, 1103.3396; found, 1103.3384. Anal. Calcd for C<sub>61</sub>H<sub>44</sub>BF<sub>2</sub>IrN<sub>6</sub>·5CH<sub>2</sub>Cl<sub>2</sub>·2.4C<sub>6</sub>H<sub>14</sub> (C<sub>6</sub>H<sub>14</sub>: hexane): C, 55.71; H, 5.09; N, 4.85. Found: C, 55.37; H, 5.42; N, 5.15.

**Ir2.** A red powder was obtained as the product (yield: 30%). <sup>1</sup>H NMR (400 MHz, CDCl<sub>3</sub>) δ 8.40 (d, *J* = 5.2 Hz, 1H), 8.30 (d, *J* = 5.5 Hz, 1H), 8.18 (d, *J* = 8.1 Hz, 1H), 8.04 (d, *J* = 8.0 Hz, 1H), 7.97 (d, *J* = 7.8 Hz, 1H), 7.83 (d, *J* = 7.9 Hz, 1H), 7.78 (d, *J* = 8.7 Hz, 1H), 7.69 (d, *J* = 8.7 Hz, 1H), 7.60–7.40 (m, 4H), 7.35 (t, *J* = 8.1 Hz, 2H), 7.22 (d, *J* = 6.6 Hz, 6H), 7.10 (ddd, *J* = 22.5, 14.7, 6.6 Hz, 4H), 6.89 (d, *J* = 6.9 Hz, 1H), 6.79 (d, *J* = 8.3 Hz, 1H), 6.43 (s, 1H), 6.26 (d, *J* = 7.3 Hz, 1H), 5.91 (s, 1H), 3.28 (s, 3H), 2.52 (s, 3H), 2.15 (s, 3H), 1.33 (s, 3H), 1.26 (s, 3H). ESI-HRMS (*m/z*): calcd. for [C<sub>59</sub>H<sub>44</sub>BF<sub>2</sub>IrN<sub>6</sub>+H]<sup>+</sup>, 1079.3396; found, 1079.3389. Anal. Calcd for C<sub>59</sub>H<sub>44</sub>BF<sub>2</sub>IrN<sub>6</sub>·0.4CH<sub>2</sub>Cl<sub>2</sub>·0.6C<sub>6</sub>H<sub>14</sub>: C, 65.02; H, 4.61; N, 7.22. Found: C, 64.62; H, 4.92; N, 7.19.

**Ir3.** A dark purple powder was obtained as the product (yield: 56%). <sup>1</sup>H NMR (400 MHz, CDCl<sub>3</sub>) δ 9.36 (d, *J* = 5.4 Hz, 1H), 8.39 (d, *J* = 5.9 Hz, 1H), 8.27 (dd, *J* = 12.3, 7.0 Hz, 2H), 8.16 (d, *J* = 8.5 Hz, 1H), 8.03 (dd, *J* = 16.6, 8.0 Hz, 2H), 7.83 (d, *J* = 8.3 Hz, 1H), 7.74 (t, *J* = 8.2 Hz, 2H), 7.68 (d, *J* = 8.8 Hz, 1H), 7.56–7.47 (m, 3H), 7.39–7.26 (m, 4H), 7.25–7.00 (m, 6H), 6.87 (d, *J* = 1.8 Hz, 1H), 6.81 (t, *J* = 7.6 Hz, 1H), 6.68 (d, *J* = 7.0 Hz, 1H), 6.28 (d, *J* = 7.0 Hz, 1H), 5.98 (d, *J* = 7.1 Hz, 1H), 4.37–4.17 (m, 2H), 3.75 (dd, *J* = 10.5, 5.7 Hz, 2H), 3.39–3.32 (m, 2H), 3.29 (s, 3H), 3.02–2.83 (m, 2H), 2.75–2.59 (m, 2H), 2.59 (s, 3H), 2.52 (s, 3H), 2.40 (dd, *J* = 4.1, 2.8 Hz, 2H), 1.36 (s, 3H), 1.32 (s, 3H). ESI-HRMS (*m/z*): calcd. for [C<sub>67</sub>H<sub>56</sub>BF<sub>2</sub>IrN<sub>6</sub>O<sub>3</sub>+H]<sup>+</sup>, 1235.4183; found, 1235.4164. Anal. Calcd for C<sub>67</sub>H<sub>56</sub>BF<sub>2</sub>IrN<sub>6</sub>O<sub>3</sub>·1.6CH<sub>2</sub>Cl<sub>2</sub>·0.3C<sub>6</sub>H<sub>14</sub>: C, 60.57; H, 4.58; N, 6.02. Found: C, 60.74; H, 4.55; N, 5.75.

**Ir4.** A dark purple powder was obtained as the product (yield: 57%). <sup>1</sup>H NMR (400 MHz, CDCl<sub>3</sub>) δ 8.27 (d, *J* = 4.6 Hz, 1H), 8.20 (d, *J* = 5.5 Hz, 1H), 8.06 (d, *J* = 8.7 Hz, 1H), 8.02–7.93 (m, 2H), 7.79–7.68 (m, 3H), 7.54–7.42 (m, 5H), 7.38 (t, *J* = 8.4 Hz, 1H), 7.30 (dd, *J* = 11.9, 7.4 Hz, 2H), 7.22 (dd, *J* = 6.5, 3.1 Hz, 3H), 7.11–6.95 (m, 5H), 6.75 (d, *J* = 5.7 Hz, 1H), 6.68 (dd, *J* = 11.5, 7.1 Hz, 2H), 6.28 (d, *J* = 7.1 Hz, 1H), 5.98 (s, 1H), 3.19 (s, 3H), 2.64 (s, 3H), 2.52 (s, 3H), 1.43 (s, 3H), 1.34 (s, 3H). ESI-HRMS (*m/z*): calcd. for [C<sub>61</sub>H<sub>44</sub>BF<sub>2</sub>IrN<sub>6</sub>+H]<sup>+</sup>, 1103.3396; found, 1103.3385. Anal. Calcd for C<sub>61</sub>H<sub>44</sub>BF<sub>2</sub>IrN<sub>6</sub>·4.8CH<sub>2</sub>Cl<sub>2</sub>·2C<sub>6</sub>H<sub>14</sub>: C, 55.55; H, 4.89; N, 5.00. Found: C, 55.46; H, 5.14; N, 5.26.

**Ir5.** A dark purple powder was obtained as the product (yield: 65%). <sup>1</sup>H NMR (400 MHz, CDCl<sub>3</sub>) δ 8.34 (d, *J* = 5.5 Hz, 1H), 8.25 (d, *J* = 5.4 Hz, 1H), 8.11 (d, *J* = 8.5 Hz, 1H), 8.07–8.03 (m, 1H), 8.02–7.98 (m, 1H), 7.83 (dd, *J* = 14.7, 8.1 Hz, 1H), 7.75 (dd, *J* = 8.9, 2.0 Hz, 2H), 7.67 (d, *J* = 1.9 Hz, 1H), 7.59–7.46 (m, 5H), 7.46–7.27 (m, 5H), 7.17–7.00 (m, 5H), 6.80 (dd, *J* = 5.1, 3.6 Hz, 1H), 6.74 (t, *J* = 7.6 Hz, 1H), 6.67 (dd, *J* = 6.2, 2.5 Hz, 1H), 6.29 (dd, *J* = 6.3, 3.3 Hz, 1H), 6.04 (s, 1H), 4.31–4.24 (m, 2H), 3.77–3.71 (m, 2H), 3.42–3.37 (m, 2H), 3.33–3.29 (m, 2H), 3.27 (s, 3H), 3.25–3.22 (m, 2H), 2.96–2.85 (m, 2H), 2.70 (s, 3H), 2.58 (s, 3H), 1.50 (s, 3H), 1.40 (s, 3H). ESI-HRMS (*m/z*): calcd. for [C<sub>67</sub>H<sub>56</sub>BF<sub>2</sub>N<sub>6</sub>O<sub>3</sub>Ir+H]<sup>+</sup>, 1235.4183; found, 1235.4169. Anal. Calcd for C<sub>67</sub>H<sub>56</sub>BF<sub>2</sub>IrN<sub>6</sub>O<sub>3</sub>·0.3H<sub>2</sub>O: C, 64.92; H, 4.60; N, 6.78. Found: C, 64.97; H, 4.77; N, 6.49.

#### 2.5. Photophysical studies.

The spectroscopic grade solvents used for photophysical studies were purchased from VWR International and used as received without further purification. The ultraviolet–visible (UV–vis) absorption spectra of complexes **Ir1–Ir5** were measured on a Varian Cary 50 spectrophotometer. Steady–state emission spectra of complexes **Ir1–Ir5** were recorded using a HORIBA FluoroMax 4 fluorometer/phosphorometer. The relative actinometry method was used for measuring the emission quantum yields of **Ir1–Ir5**. [Ru(bpy)<sub>3</sub>]Cl<sub>2</sub> in degassed acetonitrile ( $\lambda_{\max} = 436$  nm,  $\Phi_{\text{em}} = 0.097$ )<sup>61</sup> was used as the reference. The nanosecond transient absorption (TA) measurements, *i.e.* the TA spectra, triplet lifetimes, and quantum yields, were carried out on a laser flash photolysis spectrometer (Edinburgh LP920). The excitation source was the third–harmonic output (355 nm) of a Quantel Brilliant Nd:YAG laser (pulse duration, 4.1 ns;

repetition rate was 1 Hz). Before measurement, each sample solution was purged with nitrogen for 40 min. The singlet depletion method was followed to calculate the triplet excited-state molar extinction coefficients ( $\epsilon_T$ ),<sup>62</sup> and the relative actinometry method<sup>63</sup> was used to estimate the triplet excited-state quantum yields using SiNc in benzene as the reference ( $\epsilon_{590} = 70,000 \text{ M}^{-1}\text{cm}^{-1}$ ,  $\Phi_T = 0.20$ ).<sup>64</sup>

## 2.6. Computational methodology.

The ground state geometries were optimized using the Density Functional Theory (DFT)<sup>65</sup> employing PBE1 functional<sup>66</sup> and the mixed basis set, where LANL2DZ<sup>67</sup> was used for Ir(III) to incorporate the effective core potential for a heavy element and 6-31G\*<sup>68</sup> basis set was used for all remaining atoms. The solvent effects were modeled by the Conductor-like Polarizable Continuum Model (CPCM) reaction field method<sup>69</sup> for toluene.

Linear response time dependent DFT (TDDFT)<sup>70</sup> was employed to calculate excited state properties of the complexes by using the same functional and basis set that were used for the ground state calculations. It was previously reported for other Ir(III) complexes that both the ground and excited state calculations using this methodology show good agreement with the experimental results,<sup>71</sup> which defined our choice of the methodology. To meet the same energy range of the experimental absorption spectra, the lowest 80 states were calculated by TDDFT. The thermal linewidths of spectra were obtained using Gaussian function with the broadening parameter of 0.08 eV, which well fits to the line shape of experimental absorption spectra.

To calculate the emission energies, we have optimized the triplet excited state using the analytical gradient method based on TDDFT, within PBE1 functional and the mixed LANL2DZ/6-31G\* basis set. To get a better understanding of the nature of the transitions, natural transition orbitals (NTOs)<sup>72</sup> were calculated, which is the compact representation of the excited electron-hole pair obtained from the transition density matrices calculated by TDDFT. NTOs were visualized by VMD<sup>73</sup> software using 0.02 iso resolution. All quantum chemical calculations were performed using the Gaussian09<sup>®</sup> software package.<sup>74</sup>

## 2.7. Photobiological activity studies.

The details of the cellular assays, cell culture, cytotoxicity and photocytotoxicity cell assays, confocal microscopy, bacterial survival assays, and *in vitro* ROS generation measurements are provided in the Supporting Information.

## 3. Results and discussion

### 3.1. Electronic absorption.

The UV-vis absorption spectra of **Ir1–Ir5** were measured in toluene, CH<sub>3</sub>CN, THF, and CH<sub>2</sub>Cl<sub>2</sub> at room temperature. The spectra in toluene (the preferred solvent due to the high solubility of the neutral complexes in it) are displayed in Fig. 1, and the normalized spectra in the other solvents are provided

in ESI Fig. S1. The absorption band maxima and molar extinction coefficients are summarized in Table 1. **Ir1–Ir5** exhibited strong absorption bands with vibronic structure in the region of 280–460 nm, and broad, intense absorption bands centered between 500–600 nm. The energies and spectral features of these low-energy absorption bands resemble those of the 1,3,5,7-tetramethyl-8-phenyl-BODIPY.<sup>75</sup> However, the band maxima of **Ir1–Ir5** are approximately 30–40 nm red-shifted compared to the  $^1\pi,\pi^*$  absorption band of the 1,3,5,7-tetramethyl-8-phenyl-BODIPY, and these bands are broader than that of 1,3,5,7-tetramethyl-8-phenyl-BODIPY. These characteristics imply that the NHC ligand interacts with the BODIPY motif and there could be some charge transfer character in this band (see discussion *vide infra*).

Inserting a C≡C bond between the BODIPY motif and the phenyl ring in complex **Ir1** led to a red-shift of approximately 13-nm compared to that of complex **Ir2**. This difference was attributed to the extended  $\pi$ -conjugation within the NHC-BODIPY ligand of **Ir1**. Varying the point of attachment of BODIPY on the NHC ligand also showed a noticeable effect on the energy of the low-energy absorption band. Complex **Ir4**, with BODIPY attached at C5 of the benzimidazole ring blue shifted the low-energy absorption band by approximately 8 nm compared to the corresponding band in **Ir1**, where BODIPY is appended at C4 of the phenyl ring. Replacement the methyl substituents on C3 of benzimidazole in complexes **Ir1** and **Ir4** by oligoether substituents as in **Ir3** and **Ir5** did not impact the energy of the low-energy absorption band but slightly attenuated the molar extinction coefficients for this transition.

To better understand the nature of the different absorption bands, time-dependent density functional theory (TDDFT) calculations were carried out for complexes **Ir1–Ir5** in toluene. As shown in ESI Fig. S1, the calculated spectra matched well with the experimental spectra. The natural transition orbitals (NTOs) corresponding to the major transitions contributing to the major absorption bands of **Ir1–Ir5** are presented in Table 2, and in ESI Tables S1 and S2.

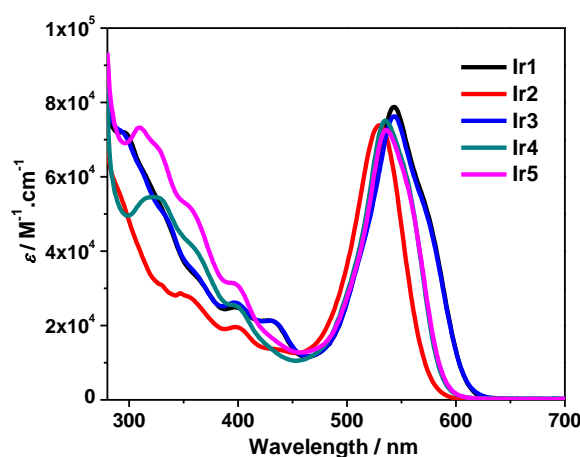


Fig. 1. UV-vis absorption spectra of **Ir1–Ir5** in toluene.



**Table 1.** Photophysical parameters for complexes **Ir1–Ir5**.

	$\lambda_{\text{abs}}/\text{nm}$ ( $\log \epsilon$ / $\text{L}\cdot\text{mol}^{-1}\cdot\text{cm}^{-1}$ ) <sup>a</sup>	$\lambda_{\text{em}}/\text{nm}$ ( $\tau_{\text{em}}/\mu\text{s}$ ); $\Phi_{\text{em}}$ <sup>b</sup>	$\lambda_{\text{T1-Tn}}/\text{nm}$ ( $\tau_{\text{TA}}/\mu\text{s}$ ; $\log \epsilon_{\text{T1-Tn}}/\text{L}\cdot\text{mol}^{-1}\cdot\text{cm}^{-1}$ ); $\Phi_{\text{T}}$ <sup>c</sup>	$\Phi_{\Delta}$ <sup>d</sup> ( $\lambda_{\text{ex}}/\text{nm}$ )
<b>Ir1</b>	294 (4.86), 335 (4.68), 352 (4.56), 398 (4.40), 430 (4.33), 543 (4.90)	610 (4.96); 0.041	457 (42.1; - <sup>e</sup> ), 679 (48.0; 4.13); 0.51	n.d. <sup>f</sup>
<b>Ir2</b>	286 (4.78), 347 (4.46), 398 (4.29), 530 (4.87)	583 (3.12); 0.063	458 (24.0; - <sup>e</sup> ), 681 (28.7; 3.83); 0.86	n.d. <sup>f</sup>
<b>Ir3</b>	290 (4.86), 335 (4.69), 352 (4.57), 397 (4.42), 430 (4.33), 543 (4.88)	610 (5.26); 0.047	455 (26.1; - <sup>e</sup> ), 690 (32.1; 4.11); 0.51	0.38 (450); 0.37 (534)
<b>Ir4</b>	322 (4.74), 350 (4.64), 396 (4.40), 535 (4.88)	587 (4.77); 0.034	449 (28.0; - <sup>e</sup> ), 699 (30.9; 4.09); 0.39	n.d. <sup>f</sup>
<b>Ir5</b>	309 (4.87), 350 (4.73), 395 (4.50), 535 (4.86)	587 (4.89); 0.010	452 (52.9; - <sup>e</sup> ), 690 (55.2; 4.06); 0.40	0.11 (352); 0.22 (450); 0.08 (534)

<sup>a</sup>Absorption band maxima ( $\lambda_{\text{abs}}$ ) and molar extinction coefficients ( $\log \epsilon$ ) in toluene at room temperature. <sup>b</sup>Emission band maxima ( $\lambda_{\text{em}}$ ), lifetimes ( $\tau_{\text{em}}$ ), and quantum yields ( $\Phi_{\text{em}}$ ) in toluene at room temperature,  $c = 1 \times 10^{-5}$  mol/L. The reference used was a degassed acetonitrile solution of  $[\text{Ru}(\text{bpy})_3]\text{Cl}_2$  ( $\Phi_{\text{em}} = 0.097$ ,  $\lambda_{\text{ex}} = 436$  nm)<sup>61</sup>. The emission lifetimes reported are the longer-lived <sup>3</sup>ILCT/<sup>3</sup>MLCT phosphorescence lifetimes. The short-lived <sup>1</sup>IL fluorescence lifetimes were unable to be reliably measured due to the resolution of our instrument. <sup>c</sup>Nanosecond TA band maxima ( $\lambda_{\text{T1-Tn}}$ ), triplet excited-state lifetimes ( $\tau_{\text{TA}}$ ), triplet extinction coefficients ( $\log \epsilon_{\text{T1-Tn}}$ ), and quantum yields ( $\Phi_{\text{T}}$ ) measured in toluene at room temperature. SiNc in benzene ( $\epsilon_{590} = 7 \times 10^4$  L mol<sup>-1</sup>cm<sup>-1</sup>,  $\Phi_{\text{T}} = 0.20$ )<sup>64</sup> was used as the reference for calculating  $\Phi_{\text{T}}$ . <sup>d</sup>Singlet oxygen quantum yields ( $\Phi_{\Delta}$ ) were measured in acetonitrile and are corrected to within  $\pm 5\%$ . <sup>e</sup>Not determined due to strong ground-state absorption, which does not satisfy the condition to apply singlet depletion method for estimation of  $\epsilon_{\text{T1-Tn}}$ . <sup>f</sup>Not determined.

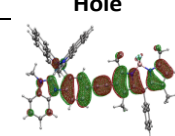
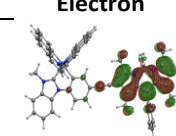
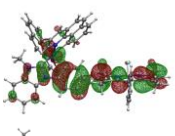
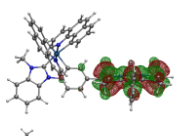
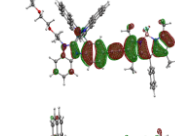
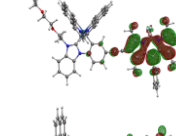
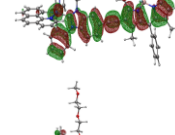
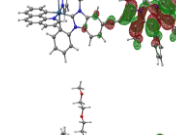
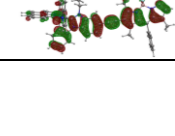
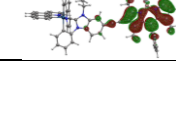
As the NTOs in Table 2 indicated, the electrons of the  $S_1$  states were almost exclusively localized on the BODIPY moiety, while the holes were delocalized on the entire BODIPY-substituted NHC ligands and on the metal  $d$  orbitals. Therefore, the  $S_1$  states in **Ir1–Ir5** have the mixed  $^1\pi, \pi^*$  / <sup>1</sup>ILCT (intraligand charge transfer,  $\pi(\text{NHC}) \rightarrow \pi^*(\text{BODIPY})$ ) / <sup>1</sup>MLCT (metal-to-ligand charge transfer,  $d(\text{Ir}) \rightarrow \pi^*(\text{BODIPY})$ ) configurations, which contributed to the intense low-energy absorption bands. For the absorption band(s) in the 370–450 nm region, the NTOs in ESI Table S1 suggest major ligand-to-ligand charge transfer (<sup>1</sup>LLCT,  $\pi(\text{bhq}) \rightarrow \pi^*(\text{BODIPY})$ ) / <sup>1</sup>MLCT transitions, admixing with some BODIPY-NHC localized <sup>1</sup>IL (intraligand transition, *i.e.*  $^1\pi, \pi^*$  / <sup>1</sup>ILCT) characters. In contrast, according to the NTOs shown in Table S2, the high energy, strong absorption bands at 280–370 nm can be predominantly assigned to the spin-allowed  $\text{bhq}$  or BODIPY-NHC ligand-centered  $^1\pi, \pi^*$  transitions, mixed with <sup>1</sup>LLCT, <sup>1</sup>MLCT, and minor <sup>1</sup>ILCT configurations.

### 3.2. Photoluminescence.

The steady-state emission spectra for complexes **Ir1–Ir5** were measured in degassed toluene, CH<sub>3</sub>CN, THF, and dichloromethane at room temperature. The normalized emission spectra in toluene are presented in Fig. 2, and the emission maxima and lifetimes are compiled in Table 1. The normalized emission spectra and the emission data in other solvents are provided in ESI Fig. S3 and Table S3. As shown in Fig. 2, all of the complexes exhibited broad and structureless luminescence in toluene ranging from 582 to 610 nm, which were mirror images to their corresponding <sup>1</sup>IL absorption bands. The emission signals showed bi-exponential decays, with a short

lifetimes of several nanoseconds and a longer lifetimes of several microseconds. The emission was only partially quenched by air. These characteristics imply that the emission of these complexes could be mixed with <sup>1</sup>IL fluorescence and charge transfer phosphorescence (<sup>3</sup>CT). This fluorescence/phosphorescence mixing has been reported for a cationic dinuclear Ir(III) complex linked by BODIPY.<sup>41</sup>

**Table 2.** NTOs for lowest-energy transitions of complexes **Ir1–Ir5** in toluene.

	$S_n$	Hole	Electron
<b>Ir1</b>	$S_1$ 533 nm $f = 0.633$		
<b>Ir2</b>	$S_1$ 480 nm $f = 0.507$		
<b>Ir3</b>	$S_1$ 531 nm $f = 0.647$		
<b>Ir4</b>	$S_1$ 515 nm $f = 0.655$		
<b>Ir5</b>	$S_1$ 513 nm $f = 0.641$		



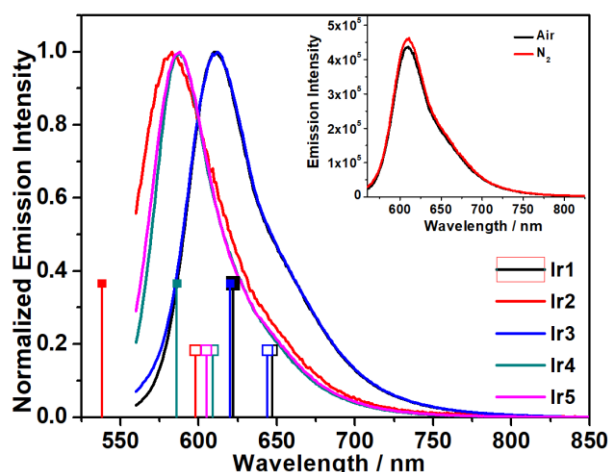


**Fig. 2.** Normalized experimental emission spectra of **Ir1–Ir5** in deaerated toluene at room temperature. The excitation wavelength was 543 nm for **Ir1** and **Ir3**, 530 nm for **Ir2**, and 535 nm for **Ir4** and **Ir5**. The open-headed lines represent the calculated  $S_1$  fluorescence and the solid-headed lines represent the calculated  $T_2$  phosphorescence. The inset shows the comparison of emission intensity in air-saturated and deaerated toluene solutions for **Ir1**.

Similar to the trend observed from the UV-vis absorption experiments, the emission maxima of **Ir1** and **Ir3** were identical to those of **Ir4** and **Ir5**, respectively. This indicates that the oligoether chain did not impact the energies of the emitting states in these complexes. In contrast, the emission of **Ir2** with BODIPY singly-bonded to NHC showed a pronounced blue-shift (27 nm) compared to that of **Ir1**, with the  $C\equiv C$  linker, due to the shorter  $\pi$ -conjugation and the reduced co-planarity between BODIPY and NHC ligand in **Ir2**. The attachment position of

BODIPY on the NHC ligand also affected the emission energy as it did for the UV-vis absorption, namely, the emission maxima of **Ir4** and **Ir5** displayed a blue-shift of 23 nm with respect to those of **Ir1** and **Ir3**.

To assign the nature of the emitting states for these complexes, TDDFT calculations were performed based on the optimized singlet triplet excited state geometries. The singlet and triplet excited-state NTOs obtained for **Ir1–Ir5** are compiled in Table 3 for  $S_1$  and  $T_2$  states, and in ESI Table S4 for  $T_1$  states. Because neither the calculated  $T_1$  energies nor the energy trend matched the experimental results, and the emission lifetimes were much shorter than the lifetimes obtained from the ns transient absorption measurement (which will be discussed in the next section), we believe that the phosphorescence components of the observed emission from these complexes are from the  $T_2$  states. Based on the NTOs provided in Table 3, the fluorescent  $S_1$  states have mixed  ${}^1ILCT/{}^1\pi, \pi^*/{}^1MLCT$  configurations, while the  $T_2$  states are predominantly  ${}^3ILCT/{}^3MLCT$  configurations mixed with minor  ${}^3\pi, \pi^*$  character. The  $S_1$  states and the  $T_2$  states are in energetic proximity, therefore, they both contribute to the observed emission. However, these two states are not in thermal equilibrium because the emission decay was bi-exponential, with a short component of less than 10 ns and a longer lifetime of several microseconds.

### 3.3. Transient absorption (TA).

To further understand the triplet excited state characteristics of **Ir1–Ir5**, especially the non-emitting  $T_1$  states in these complexes, nanosecond TA were investigated in deaerated toluene at room temperature. The TA spectra of **Ir1–Ir5** at zero-time delay upon 355-nm excitation are presented in Fig. 3. The TA parameters, such as

**Table 3.** NTOs corresponding to the optimized  $S_1$  and  $T_2$  states of complexes **Ir1–Ir5** in toluene.

	$S_1$		$T_2$			
	Energy	Hole	Electron	Energy	Hole	Electron
<b>Ir1</b>	647 nm			623 nm		
<b>Ir2</b>	598 nm			538 nm		
<b>Ir3</b>	644 nm			621 nm		
<b>Ir4</b>	609 nm			586 nm		
<b>Ir5</b>	605 nm			584 nm		

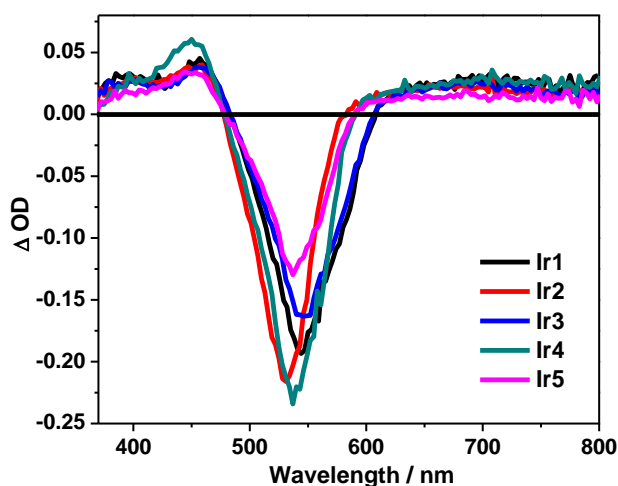


**Fig. 3.** Nanosecond transient difference absorption spectra of complexes **Ir1–Ir5** in toluene at room temperature immediately after 355 nm laser pulse excitation.  $A_{355} = 0.4$  in a 1-cm cuvette.

the TA band maxima, triplet excited-state lifetimes and quantum yields, and triplet extinction coefficients, are compiled in Table 1. Fitting of the TA signals revealed a long-lived species (ca. 28–55  $\mu\text{s}$ ). In addition, the TA spectral features of **Ir1–Ir5** were similar, with ground-state bleaching arising from the BODIPY-NHC localized  $^1\text{L}$  absorption. These spectra are also similar to that of the iodo-BODIPY reported in the literature.<sup>75</sup> Therefore, the triplet excited states that produced the observed TA should have the same nature for all of the complexes, likely from the BODIPY localized  $^3\pi, \pi^*$  state. The lifetimes of **Ir1–Ir5** obtained from the decay of the TA signals are distinctively different from their emission lifetimes, indicating that the excited states observed by TA in these complexes are different from their emitting excited states. The long TA lifetimes were assigned to excited states with  $^3\pi, \pi^*$  characters. The NTOs for  $T_1$  states in ESI Table S4 confirmed that the  $T_1$  states for these complexes are of  $^3\pi, \pi^*$  configuration and localized exclusively on the BODIPY motif.

### 3.4. Singlet oxygen generation.

**Ir3** and **Ir5** were designed with oligoether substituents as R3 (Chart 1) to increase the hydrophilicities of these neutral Ir(III) NHC complexes for improved aqueous solubility (which is a desirable property for *in vitro* biological testing). Our detailed photophysical and computational analyses of **Ir3** and **Ir5** (compared to their corresponding methyl-substituted **Ir2** and **Ir4** relatives) indicated that the addition of the oligoether groups did not alter the general excited state dynamics observed for these systems. Therefore, the more water-soluble **Ir3** and **Ir5** were further investigated for their photobiological activities.

The abilities of **Ir3** and **Ir5** to generate singlet oxygen ( $^1\text{O}_2$ ) were assessed as quantum yields for  $^1\text{O}_2$  production ( $\Phi_{\Delta}$ ) in  $\text{CH}_3\text{CN}$  relative to  $[\text{Ru}(\text{bpy})_3](\text{PF}_6)_2$  as the standard ( $\Phi_{\Delta} = 56\%$ ). The direct method was employed, whereby sensitized  $^1\text{O}_2$  was detected by its phosphorescence centered at 1268 nm.  $\text{CH}_3\text{CN}$  was used as the solvent since  $^1\text{O}_2$  phosphorescence is quenched

in aqueous solution.<sup>76</sup> The value of  $\Phi_{\Delta}$  for **Ir3** was near 37% and largely independent of excitation wavelength, whereas that for **Ir5** ranged from 8–22% as a function of excitation wavelength. Excitation at 352, 450, and 534 nm yielded values for  $\Phi_{\Delta}$  of 11, 22, and 8%, respectively.

**Ir3** was the more efficient  $^1\text{O}_2$  generator at all wavelengths investigated, which could be attributed, in part, to the fact that its quantum yield for triplet state formation is larger (51 versus 40%). Clearly, the substitution position of the BODIPY chromophore, either on the *meso*-phenyl versus the benzimidazole portion of the NHC ligand, impacts the excited state dynamics and photophysical properties of the complexes. These structural differences may, therefore, be expected to also alter their photobiological properties.

### 3.5. Cytotoxicity and photocytotoxicity toward cancer cells.

Based on their abilities to generate  $^1\text{O}_2$  under cell-free conditions, albeit with modest efficiency, it was anticipated that both **Ir3** and **Ir5** would give rise to *in vitro* photobiological effects. The human melanoma cell line SKMEL28 was used to probe the cytotoxicities and photocytotoxicities of **Ir3** and **Ir5**. Briefly, cells were dosed 1 nM–300  $\mu\text{M}$  of **Ir3** or **Ir5** (dissolved in water supplemented with 10% DMSO (v/v) and serially diluted with phosphate buffered saline (PBS)) and incubated for 16 h before receiving a dark treatment or a light treatment. The illumination condition was 100  $\text{J cm}^{-2}$  of either broadband visible or monochromatic red (625 nm) light. After a dark or light treatment, the cells were incubated for 48 h, treated with the resazurin cell viability indicator,<sup>77</sup> and incubated an additional 2–4 h. The relative cell viabilities for the dark and light treatments of cells dosed with complex were quantified by the metabolic reduction of resazurin to its fluorescent product resorufin (Fig. 4, Table 4).

**Ir3** was nontoxic toward SKMEL28 cells ( $\text{EC}_{50} > 300 \mu\text{M}$ ), while **Ir5** was substantially more cytotoxic ( $\text{EC}_{50} = 20 \mu\text{M}$ ). With broadband visible light activation, both complexes were photocytotoxic. The photocytotoxicity of **Ir5** was submicromolar, with an  $\text{EC}_{50}$  value of 150 nM and PI of 135, while the visible-light  $\text{EC}_{50}$  value for **Ir3** was approximately 10  $\mu\text{M}$  and its PI was 31. The photocytotoxicities of both complexes with red light were substantially attenuated (5-fold for **Ir3** and over 85-fold for **Ir5**), giving rise to much smaller PI values (6 for **Ir3** and 2 for **Ir5**).

**Table 4.** Comparison of  $\text{EC}_{50}$  values ( $\mu\text{M}$ ) for SKMEL28 cancer cells dosed with complexes **Ir3** and **Ir5**.

	Dark	Vis <sup>a</sup>	PI <sup>b</sup>	Red <sup>c</sup>	PI <sup>b</sup>
<b>Ir3</b>	> 300	9.66 ± 0.28	>31	53.7 ± 2.1	>6
<b>Ir5</b>	20.2 ± 1.3	0.15 ± 0.01	135	13.0 ± 0.1	2

<sup>a</sup>Vis-PDT: 16 h drug-to-light interval followed by 100  $\text{J cm}^{-2}$  broadband visible light (400–700 nm) irradiation, <sup>b</sup>PI = phototherapeutic index (ratio of dark  $\text{EC}_{50}$  to visible-light  $\text{EC}_{50}$ ), <sup>c</sup>Red-PDT: 16 h drug-to-light interval followed by 100  $\text{J cm}^{-2}$  light irradiation with 625 nm LEDs.

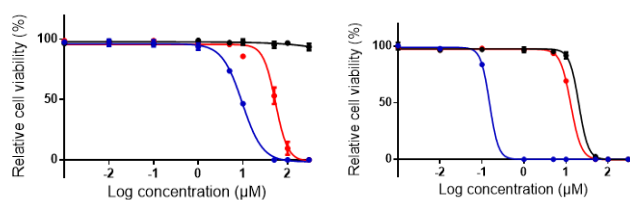


**Fig. 4.** *In vitro* dose-response curves for complexes **Ir3** (left) and **Ir5** (right) in SKMEL28 cells treated in the dark (black) and with visible (blue) or red (red) light activation.

Despite having much higher cytotoxicity in the dark, **Ir5** was the better *in vitro* photosensitizing agent according to both the magnitude of its photocytotoxicity and its phototherapeutic margin. This was initially surprising since the value of  $\Phi_{\Delta}$  for **Ir3** was significantly larger than that for **Ir5**. This discrepancy could be due to differences in  $^1\text{O}_2$  production under cell-free conditions versus the *in vitro* experiment, or that reactive oxygen species (ROS) other than  $^1\text{O}_2$  may be involved in the phototoxic mechanism, or due to different cell uptake.

To probe for the involvement of ROS, more broadly defined, as a possible source of the photocytotoxic activity for **Ir3** and **Ir5**, SKMEL28 cells were preincubated with the cell-permeable and highly sensitive 2',7'-dichlorodihydrofluorescein diacetate (DCFDA) fluorogenic dye before performing (photo)cytotoxicity assays (Fig. 5). The compounds were tested in the range of 4 pM to 126  $\mu\text{M}$ , and a sub-lethal light dose of  $50 \text{ J cm}^{-2}$  broadband visible light was used for the light condition with a reduced incubation time of 30 min between compound addition and light treatment. DCFDA is deacetylated by cellular esterases to a nonfluorescent compound, which is subsequently oxidized by ROS to the highly fluorescent DCF product that can be detected by its characteristic emission.<sup>78</sup> ROS that can be detected by this method include superoxide anion ( $\text{O}_2^{\cdot-}$ ), hydrogen peroxide ( $\text{H}_2\text{O}_2$ ), hydroxyl radical ( $\text{HO}^{\cdot}$ ), and singlet oxygen ( $^1\text{O}_2$ ), which react directly or indirectly with the deacetylated probe.<sup>79</sup>

Dark treatments were included to quantify baseline ROS levels under the assay conditions for comparison, and *tert*-butyl hydrogen peroxide (TBHP) was used as a positive control (Fig. 5c). The signal produced by TBHP was relatively weak, but sufficient, owing to the short incubation that was necessary to ensure a sub-lethal treatment with photoactivated **Ir3** and **Ir5**. ROS generation with **Ir3** in the dark was minimal at all concentrations tested, while cells treated with **Ir5** in the dark showed elevated ROS levels at concentrations greater than 1  $\mu\text{M}$ . This observation may account for the cytotoxicity induced

by **Ir5** in the absence of a light trigger, whereby **Ir5** was at least 15 $\times$  more cytotoxic (in the dark) than **Ir3**.

Light-treated complexes **Ir3** and **Ir5** increased the detected fluorescence from the DCF product in a dose-dependent manner over the dark controls and also in comparison to the positive control TBHP (Fig. 5). The highest concentration of light-treated **Ir5** (126  $\mu\text{M}$ ) showed a slight decrease in the DCF fluorescence relative to the second highest concentration (39  $\mu\text{M}$ ). This attenuation is typical when the cells begin to lose viability, which is why it is important to choose a sub-lethal dose for ROS quantification. **Ir5** produced significantly more DCF fluorescence than **Ir3** at the highest concentrations tested.

It is possible that the much larger PI measured for **Ir5** (compared to **Ir3**) may stem from its more efficient light-mediated ROS production. ROS other than  $^1\text{O}_2$  could be involved based on the lower value of  $\Phi_{\Delta}$  measured for **Ir5** under the cell-free condition. However, the level of DCF fluorescence is only raised at relatively high PS concentrations, which seems to indicate the absence of a good correlation between photocytotoxicity and widespread redox imbalance. It seems more likely that the large difference in phototoxic effects for **Ir3** and **Ir5** stems from factors that were not directly probed as part of this study, including differences in the biological target(s) for each PS and possibly contact-mediated interactions with such targets.<sup>80</sup>

Confocal microscopy was used to observe the qualitative effects of **Ir3** and **Ir5** on SKMEL28 cells with a dark or visible light treatment of  $50 \text{ J cm}^{-2}$  (Fig. 6). A concentration of 50  $\mu\text{M}$  was chosen because a marked difference in the dark cytotoxicity of **Ir3** and **Ir5** at this concentration was anticipated (since 50  $\mu\text{M}$  is greater than the dark  $\text{EC}_{50}$  value of **Ir3**, but not of **Ir5**). The light treatment was chosen to be  $50 \text{ J cm}^{-2}$  (half the dose of the cell cytotoxicity assays) and imaging was done at 15 min post-treatment to ensure that cells were imaged under sub-lethal conditions, where a comparison of cellular morphologies and uptake might be made.

The differences in the  $^3\text{MLCT}$  emission quantum yields for **Ir3** and **Ir5** were apparent in the dark confocal images, where cellular uptake by **Ir3** was detectable as a very weak signal but no signal was detected for **Ir5**. Qualitatively, there appeared to be more cellular debris from dead and dying cells treated with **Ir5** in the dark (Fig. 6a, bottom row) but emission was not detected. Both compounds caused a general change in the morphology of a large fraction of the cells treated in the dark, from the typical elongated and spindle shape to spherical.

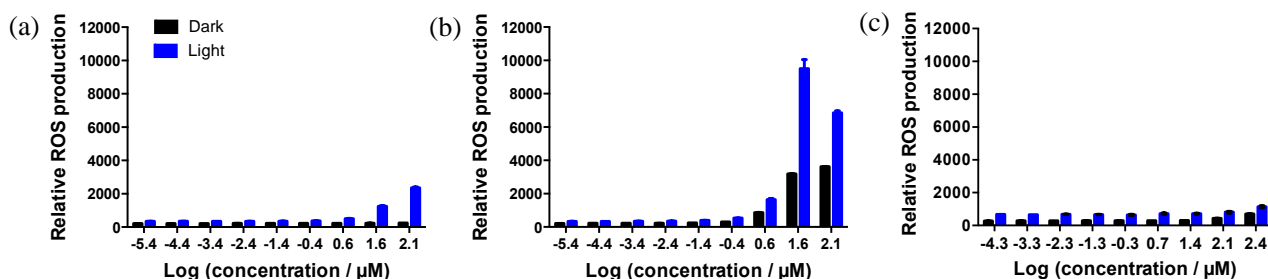


**Fig. 5.** Reactive oxygen species assay results for SKMEL28 cells treated with **Ir3** (a), **Ir5** (b), or the positive control *tert*-butyl hydrogen peroxide TBHP (c) using DCFDA as a ROS probe. Cells were treated in the dark (black bars) or with 50 J cm<sup>-1</sup> visible light (blue bars). ROS production was measured at 120 min post-treatment.

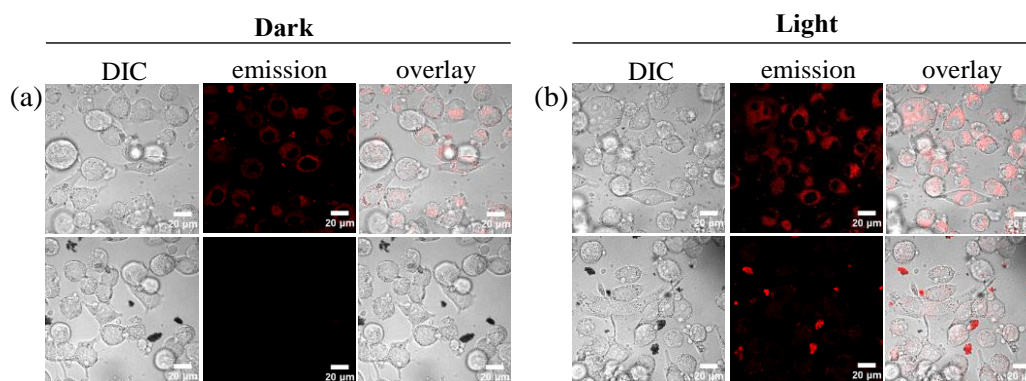


**Fig. 6.** Laser scanning confocal microscopy images of SKMEL28 cells dosed with 50 μM **Ir3** (top row) or **Ir5** (bottom row) in the dark (a) or with 50 J cm<sup>-2</sup> visible light (b).

With light activation, intracellular emission from **Ir3** was much more pronounced (Fig. 6b, top row). If the signal intensity is proportional to concentration, then photoactivated uptake of **Ir3** results in accumulation in the cytoplasm and mitochondria but not in the nuclei. Interestingly, **Ir5** produced luminescence in the cellular debris from dead and dying cells that were treated with visible light and very faint luminescence from the intact cells. Images of cells treated with **Ir3** and light did not exhibit the dark clumps of cellular debris that were observed in the images of **Ir5**, possibly reflecting the differences in photocytotoxicities and/or aggregation properties (in the presence of cellular remains) of these two complexes.

Photoactivated uptake also led to a larger concentration of **Ir5** in cells (assuming that signal intensity is proportional to concentration), making its detection possible. Given that luminescence from **Ir3** is almost five-fold more efficient than that from **Ir5** (and this difference could be magnified in cells), the confocal imaging experiment cannot definitively establish that cellular uptake of **Ir3** is higher than **Ir5**. In addition, the Stokes shift associated with **Ir3** is larger than that of **Ir5**, where inner-filter effects could contribute to the lower signal intensity associated with **Ir5**. It would be expected that the higher dark toxicity of **Ir5** would be correlated with better cellular uptake, but additional intracellular compound quantification methods were not carried out as part of this study.

### 3.6. Cytotoxicity and photocytotoxicity toward bacteria.

The antimicrobial photobiological activities of **Ir3** and **Ir5** were also assessed using *Staphylococcus aureus* (*S. aureus*) growing as planktonic cultures (Table 5, Fig. 7). The complexes were tested at concentrations between 0.4 and 100 μM, and the light treatments were approximately 35 J cm<sup>-2</sup> of visible light. Despite

showing photobiological activity against SKMEL28 melanoma cells, **Ir3** was inactive against *S. aureus* both in the dark and with a light treatment. On the other hand, **Ir5** was nontoxic to *S. aureus* in the dark but phototoxic with a visible light EC<sub>50</sub> of approximately 7 μM (PI > 15). Relatively few examples of metal complexes as PSs for antimicrobial PDT (aPDT) have been reported,<sup>38,81-84</sup> making **Ir5** notable in that respect.

The observation that **Ir3** was less photobiologically active (inactive) than **Ir5** against *S. aureus* agreed with the trend in cancer cells, further highlighting the discrepancy between the <sup>1</sup>O<sub>2</sub> quantum yields and phototoxicities for these two complexes. Why **Ir5** is less effective than **Ir3** is not known at this time, but it appears that factors other than <sup>1</sup>O<sub>2</sub> are also important for the phototoxic mechanism against *S. aureus*. The substitution position of the BODIPY unit on the NHC ligand clearly plays a major role in determining the biological and photobiological activities against the cell lines investigated in this study. It is plausible that their structural differences affect membrane permeabilization and contact-dependent chemical reactions such as lipid photooxidation as demonstrated by Baptista and coworkers.<sup>80</sup> Confirming this would be a critical next step for rational design of subsequent-generation PSs of this class.

**Table 5.** Comparison of EC<sub>50</sub> values (μM) for *Staphylococcus aureus* dosed with **Ir3** or **Ir5**.

	Dark	Vis <sup>a</sup>	PI <sup>b</sup>
<b>Ir3</b>	>100	>100	-
<b>Ir5</b>	>100	6.67 ± 0.07	>15

<sup>a</sup>35 J cm<sup>-2</sup> broadband visible light irradiation; <sup>b</sup>PI = phototherapeutic index (ratio of dark EC<sub>50</sub> to visible-light EC<sub>50</sub>).



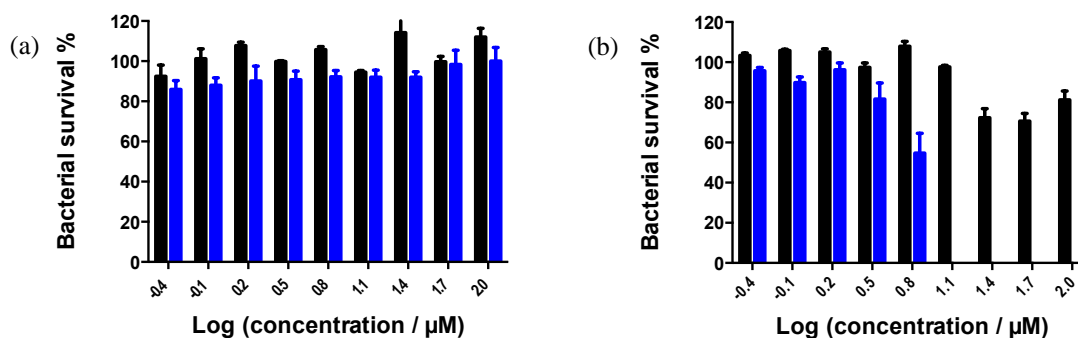


**Fig. 7.** Bacterial cell survival dose-response bar graphs for complexes **Ir3** (a) and **Ir5** (b) in *S. aureus*, treated in the dark (black) or with  $35 \text{ J cm}^{-1}$  visible (blue) light. In panel b, the bacterial survival rates were zero when **Ir5** concentrations reached  $\geq 12.5 \mu\text{M}$ , thus no blue bars were shown for those concentrations.

#### 4. Conclusions

New neutral Ir(III) complexes bearing BODIPY-substituted NHC ligands are reported. Their photophysical characteristics were systematically investigated via spectroscopic methods and DFT calculations. All complexes exhibited BODIPY-localized intense  $^1\text{L}^1\text{MLCT}$  absorption at 530–543 nm and  $^1\text{L}^3\text{CT}$  emission at 582–610 nm. However, the lowest triplet excited state of these complexes are the BODIPY-localized  $^3\pi, \pi^*$  states. It was demonstrated that the position of the BODIPY pendant on the NHC ligand impacted both the  $^1\text{L}^1\text{MLCT}$  absorption and  $^1\text{L}^3\text{CT}$  emission bands. Complexes **Ir1** and **Ir3**, with the BODIPY-ethynyl motif attached at C4 of the phenyl ring of the NHC ligand, caused a red-shift of the  $^1\text{L}^1\text{MLCT}$  absorption and  $^1\text{L}^3\text{CT}$  emission bands compared to those in **Ir4** and **Ir5** that have BODIPY-ethynyl at C5 of the benzimidazole unit of the NHC ligand. Meanwhile, both the lowest singlet excited state and the emitting states of **Ir1** were lowered compared to those in **Ir2**, due to the extended  $\pi$ -conjugation induced by the ethynyl linker in **Ir1**. In contrast, replacing the methyl substituents on C3 of benzimidazole in complexes **Ir1** and **Ir4** by oligoether substituents in **Ir3** and **Ir5**, respectively, did not impact the energies of the lowest singlet and emitting excited states in the corresponding complexes.

**Ir3** and **Ir5** were photobiologically active toward SKMEL28 melanoma cells with visible light activation, with **Ir5** possessing a much larger PI and higher photocytotoxicity. The photobiological trends in cancer cells did not correlate with cell-free  $^1\text{O}_2$  quantum yields. The DCFDA assay for intracellular ROS detection argued against a correlation between phototoxicity and widespread redox imbalance, but did show that **Ir5** was more effective at ROS production at the high PS concentrations. **Ir5** was also photobiologically active toward *S. aureus*, while **Ir3** was not. While ROS other than  $^1\text{O}_2$  may play a role in the phototoxic mechanism toward both cancer cells and bacterial cells, we hypothesize that factors such as cell membrane permeabilization and contact-mediated photooxidation reactions could be more important.

These studies indicate that the substitution position of BODIPY on the NHC ligand plays a profound role in the cytotoxicity and photocytotoxicity of this new class of complexes. C4-phenyl substitution of BODIPY compared to

substitution at C5 of benzimidazole leads to lower  $^1\text{O}_2$  quantum yields but more effective phototoxic effects. Obviously, the impact of BODIPY substitution position at the NHC ligand is more pronounced on the photobiological activities than on the photophysical properties. Future studies are aimed at quantifying the interaction of the **Ir3** and **Ir5** with cells to better understand their stark differences in photocytotoxicity, which is a critical next-step toward establishing structure-activity relationships and expanding this new class of neutral Ir(III) NHC complexes.

#### Conflicts of interest

There are no conflicts to declare.

#### Acknowledgements

W. Sun and S. Kilina acknowledges the financial support from the National Science Foundation (DMR-1411086) for materials synthesis, characterization and computational simulation of the optical spectra. For computational resources and administrative support, authors thank the Center for Computationally Assisted Science and Technology (CCAST) at North Dakota State University. The photobiological research reported in this publication was supported by the National Cancer Institute of the National Institutes of Health under Award Number R01CA222227. The content is solely the responsibility of the authors and does not necessarily represent the official views of the National Institutes of Health. S. A. M. also acknowledges support from the University of North Carolina at Greensboro, the Natural Sciences and Engineering Council of Canada, the Canadian Foundation for Innovation, the Nova Scotia Research and Innovation Trust, and Acadia University. We also thank Huimin Yin at Acadia University for her help in the photobiological studies.

#### References

- 1 J. P. Celli, B. Q. Spring, I. Rizvi, C. L. Evans, K. S. Samkoe, S. Verma, B. W. Pogue and T. Hasan, Imaging and photodynamic therapy: mechanisms, monitoring, and optimization, *Chem. Rev.*, 2010, **110**, 2795–2838.

- X. Li, S. Lee and J. Yoon, Supramolecular photosensitizers rejuvenate photodynamic therapy, *Chem. Soc. Rev.*, 2018, **47**, 1174–1188.
- D. E. J. G. J. Dolmans, D. Fukumura and R. K. Jain, Photodynamic therapy for cancer, *Nat. Rev. Cancer*, 2003, **3**, 380–387.
- W. M. Sharman, C. M. Allen and J. E. van Lier, Photodynamic therapeutics: basic principles and clinical applications, *Drug Disc. Today*, 1999, **4**, 507–517.
- J. Moan and Q. Peng, An outline of the hundred-year history of PDT, *Anticancer Res.*, 2003, **23**, 3591–3600.
- B. C. Wilson, Photodynamic therapy for cancer: Principles, *Can. J. Gastroenterol. Hepatol.*, 2002, **16**, 393–396.
- M. B. Vrouenraets, G. W. Visser, G. B. Snow and G. A. van Dongen, Basic principles, applications in oncology and improved selectivity of photodynamic therapy, *Anticancer Res.*, 2003, **23**, 505–522.
- O. J. Stacey and S. J. A. Pope, New avenues in the design and potential application of metal complexes for photodynamic therapy, *RSC Adv.*, 2013, **3**, 25550–25564.
- C. Mari, V. Pierroz, S. Ferrari and G. Gasser, Combination of Ru(II) complexes and light: new frontiers in cancer therapy, *Chem. Sci.*, 2015, **6**, 2660–2686.
- S. Monro, K. L. Colón, H. Yin, J. Roque, P. Konda, S. Gujar, R. P. Thummel, L. Lilge, C. G. Cameron and S. A. McFarland, Transition metal complexes and photodynamic therapy from a tumor-centered approach: challenges, opportunities, and highlights from the development of TLD1433, *Chem. Rev.*, 2019, **119**, 797–828.
- G. Shi, S. Monro, R. Hennigar, J. Colpitts, J. Fong, K. Kasimova, H. Yin, R. DeCoste, C. Spencer, L. Chamberlain, A. Mandel, L. Lilge and S. A. McFarland, Ru(II) dyads derived from alpha-ligandophenones: a new class of potent and versatile photosensitizers for PDT, *Coord. Chem. Rev.*, 2015, **282–283**, 127–138.
- C. Wang, L. Lystrom, H. Yin, M. Hetu, S. Kilina, S. A. McFarland and W. Sun, Increasing the triplet lifetime and extending the ground-state absorption of biscyclometalated Ir(III) complexes for reverse saturable absorption and photodynamic therapy applications, *Dalton Trans.*, 2016, **45**, 16366–16378.
- A. Zamora, G. Viguera, V. Rodríguez, M. D. Santana and J. Ruiz, Cyclometalated iridium(III) luminescent complexes in therapy and phototherapy, *Coord. Chem. Rev.*, 2018, **360**, 34–76.
- W. Lv, Z. Zhang, K. Y. Zhang, Y. Zhang, H. Yang, S. Liu, A. Xu, S. Guo, Q. Zhao and W. Huang, A mitochondria-targeted photosensitizer showing improved photodynamic therapy effects under hypoxia, *Angew. Chem. Int. Ed.*, 2016, **55**, 9947–9951.
- Y. Li, C.–P. Tan, W. Zhang, L. He, L.–N. Ji and Z.–W. Mao, Phosphorescent iridium(III)–bis–N–heterocyclic carbene complexes as mitochondria-targeted theranostic and photodynamic anticancer agents, *Biomater.*, 2015, **39**, 95–104.
- S. P.–Y. Li, C. T.–S. Lau, M.–W. Louie, Y.–W. Lam, S. H. Cheng and K. K.–W. Lo, Mitochondria-targeting cyclometalated iridium(III)–PEG complexes with tunable photodynamic activity, *Biomater.*, 2013, **34**, 7519–7532.
- K. Qiu, M. Ouyang, Y. Liu, H. Huang, C. Liu, Y. Chen, L. Ji and H. Chao, Two-photon photodynamic ablation of tumor cells by mitochondria-targeted iridium(III) complexes in aggregated states, *J. Mater. Chem. B*, 2017, **5**, 5488–5498.
- M. Ouyang, L. Zeng, K. Qiu, Y. Chen, L. Ji and H. Chao, Cyclometalated Ir<sup>III</sup> complexes as mitochondria-targeted photodynamic anticancer agents, *Eur. J. Inorg. Chem.*, 2017, **2017**, 1764–1771.
- Y. Zheng, L. He, D.–Y. Zhang, C.–P. Tan, L.–N. Ji and Z.–W. Mao, Mixed–ligand iridium(III) complexes as photodynamic anticancer agents, *Dalton Trans.*, 2017, **46**, 11395–11407.
- L. He, Y. Li, C.–P. Tan, R.–R. Ye, M.–H. Chen, J.–J. Cao, L.–N. Ji and Z.–W. Mao, Cyclometalated iridium(III) complexes as lysosome-targeted photodynamic anticancer and real-time tracking agents, *Chem. Sci.*, 2015, **6**, 5409–5418.
- J. S. Nam, M. G. Kang, J. Kang, S. Y. Park, S. J. Lee, H. T. Kim, J. K. Seo, O. H. Kwon, M. H. Lim, H. W. Rhee and T. H. Kwon, Endoplasmic reticulum-localized iridium(III) complexes as efficient photodynamic therapy agents via protein modifications, *J. Am. Chem. Soc.*, 2016, **138**, 10968–10977.
- R. Cao, J. Jia, X. Ma, M. Zhou and H. Fei, Membrane localized iridium(III) complexes induces endoplasmic reticulum stress and mitochondria-mediated apoptosis in human cancer cells, *J. Med. Chem.*, 2013, **56**, 3636–3644.
- X. Tian, Y. Zhu, M. Zhang, L. Luo, J. Wu, H. Zhou, L. Guan, G. Battaglia and Y. Tian, Localization matters: a nuclear targeting two-photon absorption iridium complex in photodynamic therapy, *Chem. Commun.*, 2017, **53**, 3303–3306.
- S. Liu, H. Liang, K. Y. Zhang, Q. Zhao, X. Zhou, W. Xu and W. Huang, A multifunctional phosphorescent iridium(III) complex for specific nuclear staining and hypoxia monitoring, *Chem. Commun.*, 2015, **51**, 7943–7946.
- G. Zhang, H. Zhang, Y. Gao, R. Tao, L. Xin, J. Yi, F. Li, W. Liu and J. Qiao, Near-infrared-emitting iridium(III) complexes as phosphorescent dyes for live cell imaging, *Organometallics*, 2014, **33**, 61–68.
- J. O. Escobedo, O. Rusin, S. Lim and R. M. Stromgim, NIR dyes for bioimaging applications, *Curr. Opin. Chem. Biol.*, 2010, **14**, 64–70.
- L. Skorka, M. Filapek, L. Zur, J. G. Matecki, W. Pisarski, M. Olejnik, W. Danikiewicz and S. Krompiec, Highly phosphorescent cyclometalated iridium(III) complexes for optoelectronic applications: fine tuning of the emission wavelength through ancillary ligands, *J. Phys. Chem. C*, 2016, **120**, 7284–7294.
- R. Liu, N. Dandu, J. Chen, Y. Li, Z. Li, S. Liu, C. Wang, S. Kilina, B. Kohler and W. Sun, Influence of different diimine (N<sup>^</sup>N) ligands on the photophysics and reverse saturable absorption of heteroleptic cationic iridium(III) complexes bearing cyclometalating 2–{3–[7–(benzothiazol–2–yl)fluoren–2–yl]phenyl}pyridine (C<sup>^</sup>N) ligands, *J. Phys. Chem. C*, 2014, **118**, 23233–23246.
- L. Wang, H. Yin, P. Cui, M. Hetu, C. Wang, S. Monro, R. D. Schaller, C. G. Cameron, B. Liu, S. Kilina, S. A. McFarland and W. Sun, Near-infrared-emitting heteroleptic cationic iridium complexes derived from 2,3-diphenylbenzo[g]quinoxaline as in vitro theranostic photodynamic therapy agents, *Dalton Trans.*, 2017, **46**, 8091–8103.
- W. Sun, C. Pei, T. Lu, P. Cui, Z. Li, C. McCleese, Y. Fang, S. Kilina, Y. Song and C. Burda, Reverse saturable absorbing cationic iridium(III) complexes bearing 2–(2–quinolinyl)quinoxaline ligand: effects of different cyclometalating ligands on the linear and nonlinear absorption, *J. Mater. Chem. C*, 2016, **4**, 5059–5072.
- Q. Zhao, S. Liu, M. Shi, C. Wang, M. Yu, L. Li, F. Li, T. Yi and C. Huang, Series of new cationic iridium(III) complexes with tunable emission wavelength and excited state properties: Structures, theoretical calculations, and photophysical and electrochemical properties, *Inorg. Chem.*, 2006, **45**, 6152–6160.
- B. Liu, L. Lystrom, S. Kilina and W. Sun, Tuning the ground state and excited state properties of monocationic iridium(III) complexes by varying the site of benzannulation on diimine ligand, *Inorg. Chem.*, 2017, **56**, 5361–5370.





- back-thinned CCD detector, *Phys. Chem. Chem. Phys.*, 2009, **11**, 9850–9860.
- 62 I. Carmichael and G. L. Hug, Triplet–triplet absorption spectra of organic molecules in condensed phases, *J. Phys. Chem. Ref. Data*, 1986, **15**, 1–250.
- 63 C. V. Kumar, L. Qin and P. K. Das, Aromatic thioketone triplets and their quenching behaviour towards oxygen and di-*t*-butylnitroxy radical. A laser–flash–photolysis study. *J. Chem. Soc., Faraday Trans. 2*, 1984, **80**, 783–793.
- 64 P. A. Firey, W. E. Ford, J. R. Sounik, M. E. Kenney and M. A. J. Rodgers, Silicon naphthalocyanine triplet state and oxygen. a reversible energy–transfer reaction, *J. Am. Chem. Soc.*, 1988, **110**, 7626–7630.
- 65 W. Kohn and L. J. Sham, Self-consistent equations including exchange and correlation effects, *Phys. Rev.*, 1965, **140**, A1133–A1138.
- 66 P. M. W. Gill, B. G. Johnson, J. A. Pople and M. J. Frisch, The performance of the Becke–Lee–Yang–Parr (B–LYP) density functional theory with various basis sets, *Chem. Phys. Lett.*, 1992, **197**, 499–505.
- 67 P. J. Hay and W. R. Wadt, Ab initio effective core potentials for molecular calculations. Potentials for K to Au including the outermost core orbitals, *J. Chem. Phys.*, 1985, **82**, 299–310.
- 68 T. Clark, J. Chandrasekhar, G. W. Spitznagel and P. V. R. Schleyer, Efficient diffuse function–augmented basis sets for anion calculations. III. The 3–21+G basis set for first–row elements, Li–F, *J. Comput. Chem.*, 1983, **4**, 294–301.
- 69 V. Barone, M. Cossi and J. Tomasi, Geometry optimization of molecular structures in solution by the polarizable continuum model, *J. Comput. Chem.*, 1998, **19**, 404–417.
- 70 M. E. Casida, C. Jamorski, K. C. Casida and D. R. Salahub, Molecular excitation energies to high-lying bound states from time–dependent density–functional response theory: characterization and correction of the time–dependent local density approximation ionization threshold, *J. Chem. Phys.*, 1998, **108**, 4439–4449.
- 71 C. Pei, P. Cui, C. McCleese, S. Kilina, C. Burda and W. Sun, Heteroleptic cationic iridium(III) complexes bearing naphthalimidyl substituents: synthesis, photophysics and reverse saturable absorption, *Dalton Trans.*, 2015, **44**, 2176–2190.
- 72 R. L. Martin, Natural transition orbitals, *J. Chem. Phys.*, 2003, **118**, 4775–4777.
- 73 W. Humphrey, A. Dalke and K. Schulten, VMD: visual molecular dynamics, *J. Mol. Graph.*, 1996, **14**, 33–38.
- 74 M. J. Frisch, G. W. Trucks, H. B. Schlegel, G. E. Scuseria, M. A. Robb, J. R. Cheeseman, G. Scalmani, V. Barone, B. Mennucci, G. A. Petersson, H. Nakatsuji, M. Caricato, X. Li, H. P. Hratchian, A. F. Izmaylov, J. Bloino, G. Zheng, J. L. Sonnenberg, M. Hada, M. Ehara, K. Toyota, R. Fukuda, J. Hasegawa, M. Ishida, T. Nakajima, Y. Honda, O. Kitao, H. Nakai, T. Vreven, J. A. Montgomery Jr., J. E. Peralta, F. Ogliaro, M. Bearpark, J. J. Heyd, E. Brothers, K. N. Kudin, V. N. Staroverov, R. Kobayashi, J. Normand, K. Raghavachari, A. Rendell, J. C. Burant, S. S. Iyengar, J. Tomasi, M. Cossi, N. Rega, J. M. Millam, M. Klene, J. E. Knox, J. B. Cross, V. Bakken, C. Adamo, J. Jaramillo, R. Gomperts, R. E. Stratmann, O. Yazyev, A. J. Austin, R. Cammi, C. Pomelli, J. W. Ochterski, R. L. Martin, K. Morokuma, V. G. Zakrzewski, G. A. Voth, P. Salvador, J. J. Dannenberg, S. Dapprich, A. D. Daniels, Ö. Farkas, J. B. Foresman, J. V. Ortiz, J. Cioslowski and D. J. Fox, Revision A.1, Gaussian, Inc., Wallingford CT, **2009**.
- 75 W. Wu, H. Guo, W. Wu, S. Ji and J. Zhao, Organic triplet sensitizer library derived from a single chromophore (BODIPY) with long-lived triplet excited state for triplet–triplet annihilation based upconversion, *J. Org. Chem.*, 2011, **76**, 7056–7064.
- 76 P. R. Ogilby and C. S. Foote, Chemistry of singlet oxygen. 42. Effect of solvent, solvent isotopic substitution, and temperature on the lifetime of singlet molecular oxygen ( $^1\Delta_g$ ), *J. Am. Chem. Soc.*, 1983, **105**, 3423–3430.
- 77 J. O'Brien, I. Wilson, T. Orton and F. Pognan, Investigation of the Alamar Blue (resazurin) fluorescent dye for the assessment of mammalian cell cytotoxicity, *Eur. J. Biochem.*, 2000, **267**, 5421–5426.
- 78 A. R. Rosenkranz, S. Schmaldienst, K. M. Stuhlmeier, W. Chen, W. Knapp and G. J. Zlabinger, A microplate assay for the detection of oxidative products using 2',7'-dichlorofluorescein diacetate, *J. Immunol. Methods*, 1992, **156**, 39–45.
- 79 N. A. Daghestanli, R. Itri and M. S. Baptista, Singlet oxygen reacts with 2',7'-dichlorodihydrofluorescein and contributes to the formation of 2',7'-dichlorofluorescein, *Photochem. Photobiol.*, 2008, **84**, 1238–1243.
- 80 I. O. L. Bacellar, M. C. Oliveira, L. S. Dantas, E. B. Costa, H. C. Junqueira, W. K. Martins, A. M. Durantini, G. Cosa, P. D. Mascio, M. Wainwright, R. Miotto, R. M. Cordeiro, S. Miyamoto and M. S. Baptista, Photosensitized membrane permeabilization requires contact-dependent reactions between photosensitizer and lipids, *J. Am. Chem. Soc.*, 2018, **140**, 9606–9615.
- 81 W. Lei, Q. Zhou, G. Jiang, B. Zhang and X. Wang, Photodynamic inactivation of *Escherichia coli* by Ru(II) complexes, *Photochem. Photobiol. Sci.*, 2011, **10**, 887–890.
- 82 S. L. Hopkins, L. Stepanyan, N. Vahidi, A. Jain, B. S. J. Winkel and K. J. Brewer, Visible light induced antibacterial properties of a Ru(II)–Pt(II) bimetallic complex, *Inorg. Chim. Acta*, 2017, **454**, 229–233.
- 83 Mariusz Mital and Zyta Ziara, Biological applications of Ru(II) polypyridyl complexes, *Coord. Chem. Rev.*, 2018, **375**, 434–458.
- 84 T. Le Gall, G. Lemerrier, S. Chevreux, K.-S. Tücking, J. Ravel, F. Thétiot, U. Jonas, H. Schönherr and T. Montier, Ruthenium(II) polypyridyl complexes as photosensitizers for antibacterial photodynamic therapy: A structure–activity study on clinical bacterial strains, *ChemMedChem*, 2018, **13**, 2229–2239.

## Table of Contents Synopsis

Neutral Ir(III) complexes bearing BODIPY-substituted *N*-heterocyclic carbene ligands exhibited moderate to strong photodynamic therapeutic effects toward SKMEL28 cells and antimicrobial activity upon broadband visible light activation.

